TECHNICAL UNIVERSITY OF MUNICH

CHAIR OF SENSOR BASED ROBOTIC SYSTEMS AND INTELLIGENT ASSISTANCE SYSTEMS

SUPERVISOR: PROF.DR. ING. ALBU-SCHÄFFER ALIN OLIMPIU

Evaluation Concept for Impedance Controlled Series Elastic Actuator Modules

---

MASTER-THESIS

Author:
Yu-Chen CHOU

Supervisor DLR:
Loeffl Christoph FLORIAN

In cooperation with:
GERMAN AEROSPACE CENTER (DLR)
Institute of Robotics and Mechatronics
Münchener Straße 20
82234 Oberpfaffenhofen-Weßling

Winter semester 2024
Submission Date: February 1, 2025

ERKLÄRUNG

gemäß §15 Abs. 5 APO in Zusammenhang mit §35 Abs. 7 Rapo

Name: Yu-Chen

Vorname: Chou

Geburtsdatum: 20.06.1999

Studiengang: Mechatronik und Robotik

Matrikel-Nr.: 03765411

Betreuer (TUM): Prof.Dr. Ing. Albu-Schäffer Alin Olimpiu

Betreuer (DLR): Loeffl Christoph Florian

Hiermit erkläre ich, das ich die Masterarbeit selbständig verfasst, noch nicht anderweitig für Prüfungszwecke vorgelegt, keine anderen als die angegeben Quellen oder Hilfsmittel benutzt, sowie wörtliche und sinngemäße Zitate als solche gekennzeichnet habe

München, 01.02.2025

Ort, Datum

yuchen

Unterschrift

Abstract

Compliant actuators, such as variable stiffness actuators (VSA), series elastic actuators (SEA), variable impedance actuators (VIA), etc., are increasingly used in robotics for applications requiring adaptability to different task requirements, energy efficiency, and safe interaction with humans and the environment. These actuators are widely employed in applications such as human-robot interaction, wearable assistive devices, and highly dynamic-legged robots. Among the various control strategies, impedance control has emerged as a favored approach for achieving safe and adaptive interaction. The upcoming humanoid robot in our institute, Claudia, designed with SEA-based flexible joints, highlights the integration of compliant actuation for energy-efficient and high-performance locomotion.

This thesis primarily focuses on proposing concepts for evaluating impedance-controlled SEA systems while also developing a new testbed for actuator parameter identification. Several metrics are introduced to assess system performance from three featured perspectives: apparent passive impedance, torque/velocity transmissibility, and energy efficiency under distrubance. The contributions of the concepts for evaluation include extending the passive impedance region (Z-region) from force-cascaded impedance control to the feedback equivalence based control (e.g., ESPi), enabling the parameter selection of impedance controller by direct and indirect retrieval methods based on Z-region, adapting the torque/velocity transmissiblity from force control to force cascaded impedance control, unification of torque/velocity transmissibility and Z-region for force cascaded impedance control. The findings provide a structured methodology for selecting optimal control parameters and actuator configurations, forming a foundation for future advancements in compliant robotic actuation.

Acknowledgments

I sincerely thank my supervisor Florian Christoph Löffel and Prof. Alin Albu-Schäffer for the opportunity to conduct my master's thesis in collaboration with DLR. I also appreciate Florian Christoph Löffel, Fabian Beck, Konrad Fründ, David Wandinger, Robert Burger and Konstantin Kondak for their support in setting up the testbed. Furthermore, I am grateful to my boyfriend, Li Yu, for his support and valuable suggestions during these time.

Contents

1 Introduction 1

1.1 Motivation / Background 1
1.2 Outline 2
1.3 Contribution 3

2 Theoretical Background 5

2.1 Motor Identification 5
2.2 Compliant Actuators 8
2.3 Compliant Control 10
2.4 SEA Performance Evaluation 16

3 Methodology and Analysis 19

3.1 Impedance Evaluation under Impedance Control 21
3.2 Force/Torque Transmissibility 30
3.3 Energy Efficiency under Disturbance 41

4 Augmented Analysis and User Case 47

4.1 Impedance Gain Selection from Passive Impedance 47
4.2 Maximum Torque Generation influenced Passive Impedance 50
4.3 Energy efficiency Results 53

5 Testbed and Identification 59

5.1 Testbed Configuration 59
5.2 Identification Results 63

6 Conclusion and Outlook **69**
6.1 Conclusion 69
6.2 Outlook 70

Appendix **73**
A Friction Models 73
B Identified friction parameters 74
C Lists of Symbols 75

Bibliography **80**

List of Abbreviations

CIC	Force Cascaded Impedance Control
DoB	Disturbance Observer
ESPi	Elastic Structure Preserving Impedance
FoB	Friction Observer
LFB	Large Force Bandwidth
mDoB	Motor Disturbance Observer
PEA	Parallel Elastic Actuator
SEA	Serial Elastic Actuator
VIA	Variable Impedance Actuator
VSA	Variable Stiffness Actuator

List of Figures

1.1 The new upcoming humanoid robot and its actuators. 2

1.2 Overall structure of the thesis. The lines indicate the relationships between the section contents. 3

2.1 Comparison of three friction models under ideal conditions: the Stribeck curve, the LuGre model, and the Wojewoda friction model. (a) Friction force as a function of velocity. (b) Friction force as a function of time. 8

2.2 (a) DLR Hand Arms System [49] (b) The first four arm joints, namely the elbow and the three shoulder joints, are implemented by Floating Spring Joints (FSJ) [50] (c) Under arm rotation is realized by a Bidirectional Antagonistic Variable Stiffness (BAVS) joint[51] . . . 10

2.3 New interaction control classification. The explicit/implicit node indicates the presence/absence of force feedback [53]. 11

2.4 (a) A schematic diagram of the SEA, and (b) its block diagram . . . 12

2.5 Force Cascaded Impedance Control block diagram 14

2.6 (a) Graphical representation of a single linear-elastic joint (b) ESπ control achieves a full Impedance behavior directly on the link. (c) ESP control achieves damping directly on the link. [67] 15

2.7 Z-region surrounded by the highest impedance controller (HIC) and the lowest impedance controller (LIC). This figure shows achievable SEA impedance ranges by modulating the gain scale GS =1 . The control gains are solved using the critically damped gain design criterion. [4] 17

3.1 Overview of the structure in Chapter 3. The dotted lines represent the relationships between the applied controllers and the metrics. . 19

3.2 Port concept of the SEA system represented as a circuit. The green color corresponds to the spring port, the orange to the load port, and the outputs of both ports are highlighted in yellow. 22

3.3 Comparison of apparent impedance at spring and load ports wrt. η_q under the CIC framework. 23

3.4 Apparent Impedance in CIC.$D_q = 2\sqrt{BK_q}$ has been selected for critically damped impedance. Three cases are evaluated: $(\eta_q < 1)$ at the spring port, and $(\eta_q > 1)$ evaluated at both the spring port and load port. 24

3.5 Apparent Impedance under the ESPi framework. The legend, D_q and three discussed cases condition are same as Fig. 3.4. 26

3.6 Comparison of Z-region at spring port (left) and load port (right) under CIC framework. 27

3.7 Comparison of Z-region Bode plots with respect to various K_p in 2D (a) and 3D (b) views. 28

3.8 Comparison of Z-region at spring port (left) and load port (right) under ESPi framework. 29

3.9 CIC block diagram with transfer function representations $(P_\tau, P_{\omega_m}, P_q)$, where the blue loop represents the outer position regulation loop, the orange loop represents the inner force tracking loop, and the green loop represents the relationship from u to ω_m. 31

3.10 MTT_τ Bode plot with desired impedance $K_q = 250$, $D_q = 2\sqrt{BK_q}$. 33

3.11 MTT_τ Bode plot with respect to (a) variable K_q and (b) variable K_p. The red plane represents 0 dB plane. The colorful surface represents the MTT_τ. Here, $K_q = 250$ and $K_p = 3$ are applied. 34

3.12 2D MTT_τ Bode plot with respect to variable K_q and K_p from Fig. 3.11. 35

3.13 MTT_ω Bode plot with respect to variable $\eta_{\tau,\omega}$. Here, $K_p = 3$ and $K_q = 250$ are applied. 37

3.14 MTT_ω wrt. $\eta_{\tau,\omega}$ and K_p(left) or K_q(right), From the blue color to red color represent the value from low to high. 38

3.15 ω_{MT} Bode plot with MTT_ω represented in green, MTT_τ in blue, and the 0 dB plane in red. Here, $K_q = 250$, $D_q = 2\sqrt{BK_q}$ and $K_p = 3$ are applied. 40

3.16 CIC diagram with transfer function P_q, P_τ, and P_d 42

3.17 ESPi control diagram with transfer functions P_q, P_d, Y_q, Y_r, and Y_τ. 44

3.18 transfer functions comparison with desired impedance $K_q = 250$, $D_q = 2\sqrt{BK_q}$. Solid lines represent G_u and dotted lines represent $G_{\dot{\theta}}$ 45

3.19 3D comparison of gain functions wrt. K_q. (a) G_u (b) $G_{\dot{\theta}}$ 46

4.1 Z^{CIC}_{spring} vs. K_q relationships at $s \rightarrow 0$ with $K_p = 7$ and $D_q = 2\sqrt{BK_q}$ for critical damping. Thick solid lines represent passive impedance bounds, thick dotted lines validate two cases ($K_q = 50$ and $K_q = 150$), and thin dotted lines correspond to desired K_q for Z_{des}. All system parameters are from Table 3.1, except K_p. 48

4.2 Z_{spring} mapped to Z_{des} via the Z-region for CIC. The line types are consistent with those in Fig. **??**. 49

4.3 Z_{spring} mapping to Z_{des} via Z-region for ESPi controller. The line types are consistent with those in Fig. 4.1. 50

4.4 Comparison of ω_{MT_τ} (a) on the 3D MTT_τ surface and (b) within the 2D Z-region Bode plot. 52

4.5 (a) ω_{MT_τ} and $\omega^{inner,lower}_{MT_\tau}$ plotted on the 3D MTT_τ. (b) 3D Z-region Bode plot integrated with ω_{MT_τ}. 54

4.6 Maximum control input under τ_{ext}, modeled as a periodic sinusoidal signal over 10 seconds. The red surface indicates the first resonance of each controller separately. The results are based on equations (3.51) and (3.58). 55

4.7 Peak power input under the same conditions as Fig. 4.6. The results are based on equations (3.53) and (3.60). 55

4.8 Response of the controlled SEA system to a sudden contact force, which occurs at $t = 1$ s. The desired K_q is set to 50. 56

4.9 Response of the controlled SEA system to a sudden contact force occurring at $t = 1$ s with respect to varying K_q. 57

4.10 Comparison of energy consumption w.r.t. K_q for CIC and ESPi . . 57

5.1 Initial Testbed: (a) Overall configuration; (b) Without shell; (c) Connection materials comparison. 59
5.2 Second Version Testbed: (a) Overall configuration; (b) Without shell; (c) Actuator with connection. 60
5.3 Final Testbed: (a) Overall setup. (b) CAD representation. 60
5.4 Relationship between hardware and software in the testbed configuration 61
5.5 (a)Identified stiffness: output torque vs displacement (b)actual stiffness in actuator 63
5.6 time-domain response (a) in the low frequency range (b) in the high frequency range. Here, the sample rate is 1kHz. 64
5.7 Fitted friction model: τ_{fric} versus time. Sample rate 100 Hz 65
5.8 Fitted friction model: τ_{fric} versus velocity. 66

List of Tables

3.1 Parameter Values 20

1 Fitted Parameters for the LuGre Model as defined in equation (3). . 74
2 Fitted Parameters for the Stribeck Model as defined in equation (2), incorporating $\tanh(\alpha v)$ for smoother behavior around zero velocity. 74
3 Fitted Parameters for the Wojewoda Model as defined in equation (4). 75

1 Introduction

1.1 Motivation / Background

In recent years, compliant actuators have gained significant popularity in the development of robotic systems and are extensively studied and widely utilized in applications such as human-robot interaction [1], energy-efficient motion [2], wearable assistive devices [3], humanoid robots [4], and highly dynamic legged robots [5]. Alongside compliant actuators, various control strategies have been implemented, including force control [6], impedance control [7], and passivity-based control [8] and so on. Among these, impedance control has become particularly favored for human interaction and adaption to unknown environments.

The upcoming humanoid robot, Claudia, developed at the institute, aims to achieve energy-efficient and high-performance legged locomotion through compliant actuation, as shown in Fig. 1.1a. The lower ankles, highlighted in the figure, feature flexible joints driven by series elastic actuators (SEAs), which absorb impacts during locomotion and exploit potential energy to reduce input power. The upper limbs of Claudia are primarily composed of similar actuator modules, with glass fiber serving as the elastic transmission element, as illustrated in Fig. 1.1b and 1.1c. To ensure accurate torque control and compensate for variations in the elastic transmission, these actuators require testing on the testbed prior to installation on Claudia.

This thesis develops a testbed for actuator parameters identification upon the presented modeling. The testbed is designed to accommodate various actuator configurations, supporting future design iterations. Additionally, we also aim to establish unified metrics for evaluating impedance-controlled SEA systems, currently focusing on the concept of evaluation from three featured perspectives: apparent

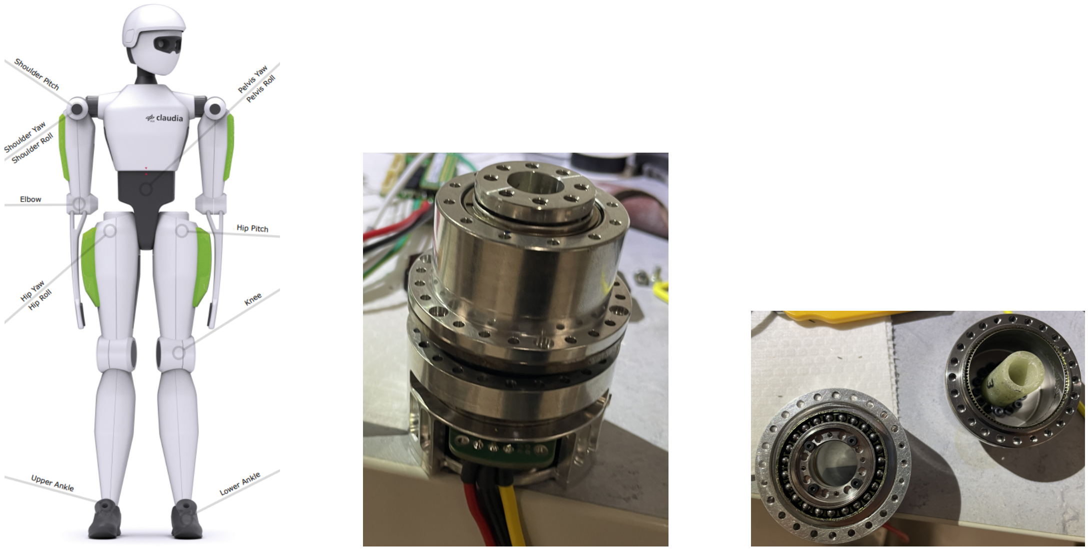
Shoulder Pitch
Shoulder Yaw
Shoulder Roll
Elbow
Hip Yaw
Hip Roll
Upper Ankle
Pelvis Yaw
Pelvis Roll
claudia
Hip Pitch
Knee
Lower Ankle

(a) Claudia robot (b) Tested Actuator (c) Tested Actuator

Figure 1.1: The new upcoming humanoid robot and its actuators.

passive impedance, torque/velocity transmissibility, and energy efficiency. These evaluations provide a basis for selecting optimal controllers, ensuring performance and interaction requirements in applications such as humanoid locomotion and energy-efficient robotic actuation.

1.2 Outline

The overall structure of this thesis, as illustrated in Fig. 1.2, is as follows: The theoretical foundation for compliant actuators, identification methods, control strategies, and metrics for evaluation is introduced in chapter 2. The concept for evaluation from three featured perspectives, along with related metrics and analyses, are presented in chapter 3. User cases of the metrics and the related approaches based on the mentioned metrics for impedance controllers design are discussed in chapter 4. The design of the testbed, including its hardware and software components, as well as the identification results and corresponding analysis, is covered in chapter 5. The summary and outlook of the thesis are provided in chapter 6.

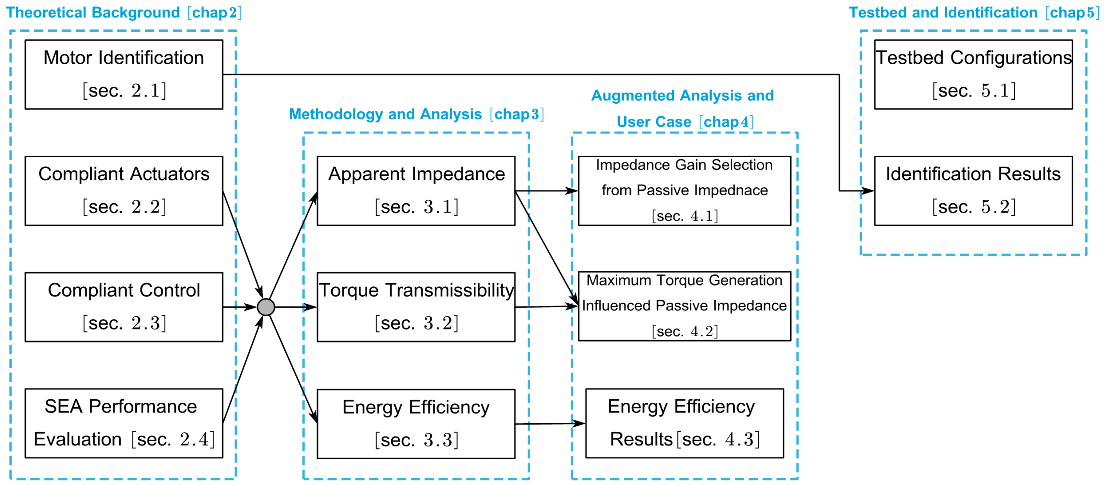
Theoretical Background [chap2]
Motor Identification [sec. 2.1]
Compliant Actuators [sec. 2.2]
Compliant Control [sec. 2.3]
SEA Performance Evaluation [sec. 2.4]
Methodology and Analysis [chap3]
Apparent Impedance [sec. 3.1]
Torque Transmissibility [sec. 3.2]
Energy Efficiency [sec. 3.3]
Augmented Analysis and User Case [chap4]
Impedance Gain Selection from Passive Impednace [sec. 4.1]
Maximum Torque Generation Influenced Passive Impedance [sec. 4.2]
Energy Efficiency Results [sec. 4.3]
Testbed and Identification [chap5]
Testbed Configurations [sec. 5.1]
Identification Results [sec. 5.2]

Figure 1.2: Overall structure of the thesis. The lines indicate the relationships between the section contents.

1.3 Contribution

This thesis advances the evaluation and control of impedance-controlled SEA systems by analyzing their performance and proposing structured methodologies for controller selection. The key contributions are as follows.

Apparent impedance of impedance controlled system is commonly evaluated by passivity whereas a regional representation of passive impedance (Z-region) enhances assessment in specific operational regions. This concept has been widely applied to force cascaded impedance control (CIC), where the constraint on desired impedance stiffness shrinks the passive impedance region. In this thesis, we extend this concept to feedback equivalence based control independent of force control, i.e. ESPi by Keppler [9] (section 3.1). Theoretically, ESPi allows unrestricted parameter selection, leading to a larger passive impedance region. The Z-region concept enables direct and indirect retrieval methods to select impedance controllers based on the passive impedance region for CIC and ESPi control proposed in section 4.1.

However, the desired passive impedance in CIC can deviate due to limitations in controlled force fidelity, which arise from the nominal maximum continuous torque and permissible velocity. To address this, torque and velocity transmissibility metrics were adapted from simple force control to CIC, resulting in an evaluation defined by feasible frequency width and maximum torque generation constraints (section 3.2). Consequently, a higher impedance stiffness and a lower torque control gain are preferable to a larger feasible frequency width. This enables the unification of torque and velocity transmissibility and Z-region to preserve the maximum torque generation (section 4.2).

Additionally, robustness quantifies the system's response to disturbances, while energy efficiency under disturbance is crucial for maintaining the desired impedance under constrained energy supply. To analyze this, the robustness from ESPi were adapted to CIC [10], providing a basis for discussing absolute power consumption and control input peaks (Section 3.3). Theoretically, the disturbances have less influence on the control input for both controllers at the anti-resonance of the controlled system, which coincides with the natural frequency of uncontrolled system. Two different disturbance cases are simulated in section 4.3.

To pursue an empiric selection and categorization of existing actuators upon versatile purposes and mechanical specification, a testbed aligned with conceptual evaluation methods are developed in mechatronics department. Finally, the actuator parameters have been identified based on the proposed modeling with designed experiments (chapter 5).

2 Theoretical Background

2.1 Motor Identification

In general, motor inertia, damping, friction, and stiffness are the key parameters to be identified in actuator models. Accurate identification enables the model to provide reliable predictions of the system's behavior under external torques. In the following, the common identification approaches will be discussed in subsection 2.1.1, followed by the basics of friction in subsection 2.1.2.

2.1.1 Identification Methods

Identification methods can be broadly categorized into offline and online approaches. Offline methods include physical experiments, CAD-based inference, and input-output behavior analysis, while online methods often utilize adaptive control or neural networks. A detailed overview of robotic dynamic parameter identification is provided in [11]. The primary objective of identification is to estimate the parameters using a minimal set of linear equations while accounting for measurement noise. Key steps involve exciting the system dynamics through specific trajectories [12, 13] and sampling input-output data to solve the equations.

Separate Parameter Identification

In this thesis, individually targeting specific parameters through separate experiments is adopted to simplify the identification process. The motor torque constant (k_T) is determined by comparing torque sensor measurements with $k_T i_{in}$ under sinusoidal excitation [14]. Elastic stiffness (K) is identified by analyzing behaviour and hysteresis during actuator motion [15].

Friction models (τ_{fric}) are identified using constant velocity measurements for static friction [15, 16, 17] and chirp signals for dynamic friction [14]. Motor inertia (B) is estimated by free rotation under constant torque with friction compensation [15], cross-correlation at maximum acceleration [14, 18], or a full-state observer with a PI speed observer [19], though the latter requires careful gain tuning and may compromise stability.

General Identification Concepts and Methods in a Single Experiments

Compared to the above-targeted experiments, identifying the entire parameter set in a single experiment is also widely used. The critical aspect lies in the different approaches to solving equations using input-output data.

Linear least squares (LS) assumes negligible noise, while weighted least squares (WLS) and maximum likelihood estimation (MLE) address noise using weighting matrices and likelihood maximization, respectively [20, 13, 12]. Advanced methods, including algebraic approaches for oscillatory systems [21] and filtered regression models to reduce noise [22], enhance accuracy. For nonlinear effects like friction and backlash, grey-box identification combines physical modeling with optimization [23, 24, 25], while black-box methods (e.g., NARX, ARX, RNN) rely solely on data but face computational and interpretability challenges [26].

Most methods operate offline, yielding static parameters. Real-time updates are crucial for handling varying parameters during operation. Iterative search routines offer a solution but often converge to local minima [27]. Achieving a global minimum relies on well-informed initial guesses, which require an understanding of parameter constraints and initial structures, making the process time-intensive.

2.1.2 Friction Basics

Friction in actuators is typically induced by mechanical gearing. Generally, classical friction models can be categorized into static and dynamic types and formulated accordingly, as discussed in [28, 29]. The following content provides a brief introduction to static and dynamic classical friction models, along with one of their variations.

Static Friction

Friction modeled statically describes the relationship between friction and contact velocity. The Coulomb friction model, as shown in Appendix A.1, represents the simplest form, with a constant frictional force depending only on the direction of motion [30]. Despite its simplicity, it fails to capture dynamic behaviors and is inaccurate near zero velocity [29].

Improved models, such as those incorporating Stribeck curves, account for nonlinear dynamics like stick-slip motion. A common Stribeck formulation uses a Gaussian expression [31], as shown in Appendix A.2, explicitly modeling the additional force needed to overcome static friction. Stick-slip occurs due to higher friction at rest compared to motion. While Stribeck models often cannot fully capture hysteresis [32], necessitating dynamic friction models for greater accuracy.

Dynamic Friction

Dynamic friction models address complex dynamics like hysteresis by incorporating differential equations with internal state variables, leveraging memory effects. The LuGre model [33], an extension of the Dahl model [34], introduces z as an internal state variable to represent the average deflection of bristles [35], detailed in Appendix A.3. This model captures rate-dependent characteristics and hysteresis but lacks reversal point memory [36].

Variation of classic models

To complement the drawbacks of other models, Wojewoda et al. introduced a friction model incorporating stochastic effects, capable of capturing complex dynamics with uneven hysteresis behavior [29]. This model, shown in Fig. 2.1 and detailed in Appendix A.4, describes irreversible motion while preserving stochastic features. A comprehensive formulation is provided in [29].

Observations across friction models

In Fig. 2.1, the ideal friction models are depicted in two views: friction versus velocity and friction versus time. On the left (Fig. 2.1a), the LuGre model exhibits a smooth hysteresis loop, while the Wojewoda model displays an uneven loop with distinct acceleration and deceleration paths. On the right (Fig. 2.1b), the Stribeck curve shows sharp corners when the force direction changes, whereas the LuGre and Wojewoda models exhibit a single corner in opposing directions.

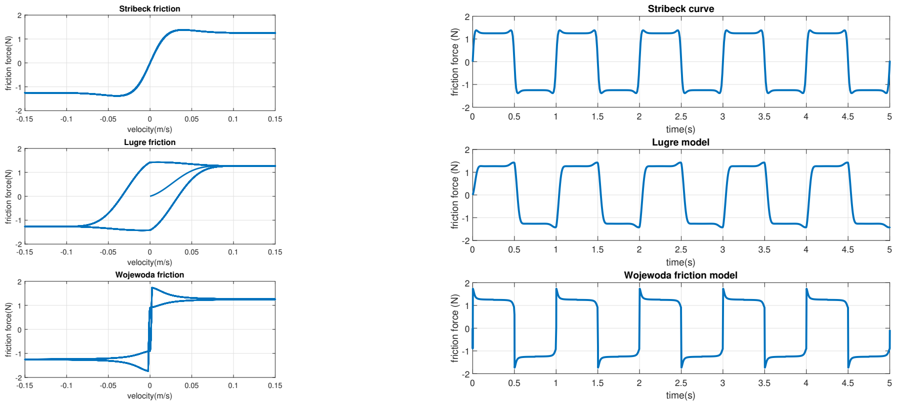

(a) Ideal friction models versus velocity

(b) Ideal friction models versus time

Figure 2.1: Comparison of three friction models under ideal conditions: the Stribeck curve, the LuGre model, and the Wojewoda friction model. (a) Friction force as a function of velocity. (b) Friction force as a function of time.

2.2 Compliant Actuators

In general, compliant actuators differ from rigid actuators by incorporating elastic elements, such as springs or deformable materials, enabling greater adaptability, energy storage, and impact resistance, particularly in dynamic or uncertain environments [37]. Nowadays, there are numerous mechanisms to integrate elastic elements into actuators, whether nonlinear, linear, constant, or variable. This section reviews the most common and widely used mechanisms.

2.2.1 Series Elastic Actuator (SEA)

The simplest mechanism is Series Elastic Actuator (SEA), which incorporates a constant elastic element to provide inherent compliance and is extensively utilized in various fields. SEAs were first introduced by Pratt in 1995 [38]. This design has gained popularity and has become a preferred choice for applications such as assistive robots (e.g., exoskeletons and prostheses), humanoid robots, and rehabilitation devices.

SEAs offer several advantages, including increased energy efficiency, as the spring stores and releases energy during operation [39], improved impact absorption, as the elastic element acts as a low-pass filter for external forces [40], and enhanced control robustness [41]. A detailed comparison of different types of SEAs, in terms of the displacement of the spring and the gear in SEAs, is provided in [42].

2.2.2 Parallel Elastic Actuator (PEA)

Complementing the series configuration in subsection 2.2.1, Parallel Elastic Actuators (PEAs), introduced by Mettin in [43], offer an alternative approach to improving actuator performance. By incorporating elastic elements in parallel with the actuator, PEAs reduce the control input required for specific motions by effectively utilizing the energy storage and return capabilities of the parallel springs [44, 45, 2, 46].

2.2.3 Variable Stiffness Actuator (VSA)

In addition to constant stiffness which have already mentioned in subsection 2.2.1 and 2.2.2, variable stiffness actuators (VSAs) have emerged as another mechanical design solution to address mentioned challenges, first introduced by Tonietti in [47]. VSAs are designed to adapt a system's natural dynamics by controlling its stiffness [48]. One example is the DLR Hand Arm System, which combines Floating Spring Joints (FSJ) for the first four arm joints and Bidirectional Antagonistic Variable Stiffness (BAVS) joints for the wrist and forearm, as shown in Fig. 2.2.

The FSJ, illustrated in Fig. 2.2(b), achieves variable stiffness through a single floating spring mechanism positioned between two cam disks, without being attached to the housing. The stiffness is adjusted by the relative motion of the cam disks [50]. In contrast, the BAVS joint, shown in Fig. 2.2(c), employs two antagonistic actuators to adjust stiffness and generate bidirectional torque by controlling the deflection of elastic elements via cam discs [51].

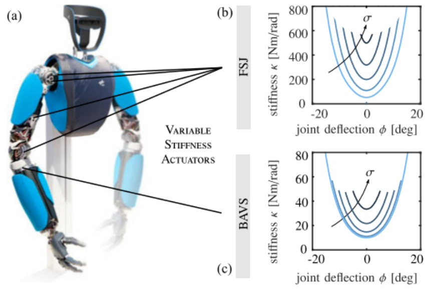

Figure 2.2: (a) DLR Hand Arms System [49] (b) The first four arm joints, namely the elbow and the three shoulder joints, are implemented by Floating Spring Joints (FSJ) [50] (c) Under arm rotation is realized by a Bidirectional Antagonistic Variable Stiffness (BAVS) joint[51]

2.2.4 Variable Impedance Actuator (VIA)

Building on the concept of VSA, Variable Impedance Actuators (VIAs) were proposed as an extension, enabling adaptation to unknown environmental dynamics by varying both stiffness and damping[1]. A detailed review of different types of VIAs and their applications can be found in [52].

2.3 Compliant Control

Interaction control is generically defined as control in an environment with kinematic and/or dynamic constraints, in contrast to motion control. There are two main categories: passive and active interaction control. Passive interaction control primarily relies on position control, where the compliance arises from the inherent structure or mechanism of the system. In contrast, active interaction control generates compliance through the actions of the controller [6]. Active interaction strategies can generally be grouped into two categories: direct force control and indirect force control. The main distinction is that the former explicitly closes the force feedback loop, while impedance/admittance control belongs to the latter.

However, when considering compliant actuators, the classification cannot be fully aligned with this logic. New classifications, as illustrated in Fig. 2.3, were introduced by Calanca in [53]. Compliant control forms the foundation of control strategies designed to handle unstructured environments safely. It is widely applied to both stiff and compliant joint systems. Generally, these controllers aim to shape the mechanical impedance of the system, which defines the relationship between output force and output velocity or position [7].

---

[1] Although impedance generally encompasses inertia, damping, and stiffness, current implementations of VIAs primarily focus on varying stiffness and damping.

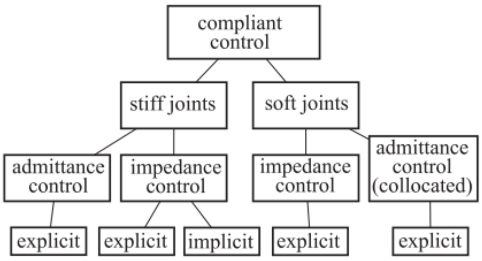
compliant control
stiff joints
soft joints
admittance control
impedance control
impedance control
admittance control (collocated)
explicit
explicit
implicit
explicit
explicit

Figure 2.3: New interaction control classification. The explicit/implicit node indicates the presence/absence of force feedback [53].

In this section, the SEA system modeling is first presented in subsection 2.3.1, followed by the foundations of force control in subsection 2.3.2. Finally, impedance control for compliant actuators is discussed in subsection 2.3.3, along with an introduction to the controllers that will be implemented in this thesis.

2.3.1 SEA Modeling

The SEA equipped a linear spring can be illustrated in Fig. 2.4(a) and structured in a block diagram shown in Fig. 2.4(b). The equations of motion utilizing a linear stiffness K_s, is give by,

$$\begin{aligned} \tau_m - \tau_{fric} &= (Bs^2 + D_m s)\theta + N^{-1}\tau_s = P_m^{-1}\theta + N^{-1}\tau_s, \\ \tau_s + \tau_{ext} &= (Ms^2 + D_l s)q = P_l^{-1}q, \\ \tau_s &= K_s(N^{-1}\theta - q) \end{aligned} \tag{2.1}$$

with

$$P_m(s) = \frac{1}{Bs^2 + D_m s}, \quad P_l(s) = \frac{1}{Ms^2 + D_l s}, \tag{2.2}$$

where τ_m represents the motor torque serves as the control input, while τ_{fric} and τ_{ext} denote the friction at the motor side and the external torque at the link side, respectively. τ_s represents the spring torque, and θ and q correspond to the motor and link displacement. For compactness, P_m and P_l have been introduced to describe the motor-side and link-side dynamics, respectively, where B and M represent the motor inertia and link inertia, while D_m and D_l denote the motor and link damping, respectively. N represents the gear ratios.

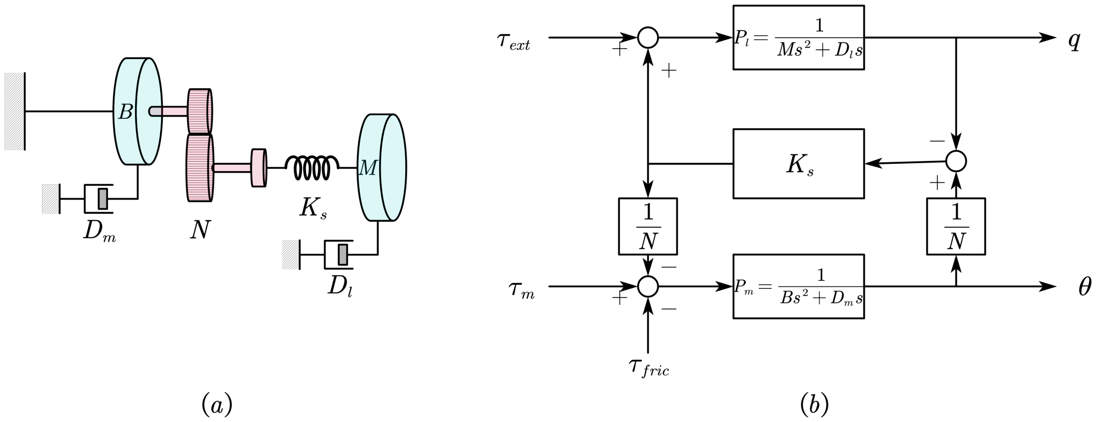

Figure 2.4: (a) A schematic diagram of the SEA, and (b) its block diagram

Alternatively, a SEA incorporating a nonlinear elastic element, the force/torque is generated by,

$$\tau_s = \boldsymbol{\phi_s}(N^{-1}\theta - q) \tag{2.3}$$

where $\boldsymbol{\phi_s}$ presents a nonlinear mapping between spring deflection and force/torque. Thus, equation (2.3) replaces the τ_s in equation (2.1). In this thesis, our discussion primarily focuses on the linear spring.

2.3.2 Force/Torque Control

The early work on force control can be found in [54, 55, 56]. Implementing a force controller requires the adoption of a stabilizing PD control action on the force error, in addition to the usual nonlinear compensation. With the force control system, the closure of an outer force regulation feedback loop is guaranteed, often accompanied by an inner position/velocity loop [57]. The force control loop can be defined as,

$$F = C_f(f_{des} - f_{out}), \tag{2.4}$$

where C_f is the force controller PD gain, f_{des} represents the desired force reference, and f_{out} is the system output force. Force/Torque control is widely used in human-robot interaction [1], compliant actuators [58, 59], exoskeletons [60], and other applications.

2.3.3 Impedance Control

In this subsection, we focus on impedance control, where impedance is mathematically defined as,

$$Z_{imp} = -\frac{\tau_{ext}}{sq} \quad \text{or} \quad -\frac{\tau_o}{sq} \tag{2.5}$$

where τ_{ext} and τ_o represent the external torque and output torque, respectively, and sq denotes the output velocity with Laplace operator s.

Impedance control, first introduced by Hogan [7], regulates the dynamic relationship between a desired trajectory and the interaction forces. Its flexibility in adapting to varying application requirements has made it a widely adopted strategy for controlling flexible joints. This adaptability allows impedance control to meet diverse demands in robotics, ranging from safety-critical tasks to precision-driven operations. For example, softer impedance is crucial in safety-critical applications such as rehabilitation devices or humanoid robots [1, 61], while stiffer impedance is preferred in scenarios requiring high-precision motion or effective disturbance rejection.

Force Cascaded Impedance Control (CIC)

Force cascaded impedance control structures shown in Fig. 2.5, are widely utilized to achieve robust and adaptive performance in robotic systems [62]. This control architecture typically consists of two hierarchical layers: an inner loop and an outer loop. The inner loop, which is commonly a velocity controller [61] or a torque controller [4, 63], is implemented using simple control strategies, such as proportional (P) or proportional-derivative (PD) controller. The outer loop serves as the impedance controller, which renders the desired impedance. To ensure system stability and responsiveness, control theory suggests that the inner loop should operate with a significantly higher control bandwidth than the outer loop [64], commonly using a factor of ten [65].

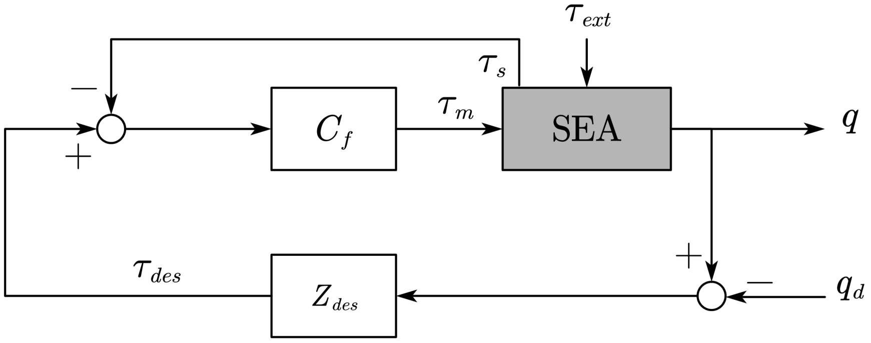

Figure 2.5: Force Cascaded Impedance Control block diagram

For torque controlled inner loop, the CIC control law

$$\tau_m = C_f(Z_{des}q - \tau_s) \tag{2.6}$$

with torque controller $C_f = K_p + K_d s$ and desired impedance $Z_{des} = -K_q - D_q s$ is taken for example.

Elastic Structure Preserving Impedance Control (ESPi)

Elastic Structure Preserving (ESP) control is one of the feedback equivalence based control, which is designed to preserve the elastic structure of the system's original plant by introducing a new coordinate on the motor side, allowing direct damping implementation on the link side [66]. One particularly notable feature of ESP control is that the proportional (P) control gain for the link side corresponds directly to the intrinsic stiffness K_s of the system, eliminating the need for gain tuning.

Elastic Structure Preserving Impedance (ESPi) control is an inversion of the ESP control structure, as depicted in Fig. 2.6. This approach enables users to directly implement the desired impedance on the link side, facilitating desired task execution or interaction scenarios [67]. The control law is formulated as,

$$\begin{aligned}\tau_m &= \bar{u} + NK_s^{-1}(P_m^{-1} + N^{-2}K_s)Z_{des}q \\ &= D_\eta\dot{\eta} + NK_s^{-1}Z_{des}(B\ddot{q} + D_m\dot{q} + N^{-2}K_s q)\end{aligned} \tag{2.7}$$

where $\bar{u} = D_\eta\dot{\eta}$ represents the new control input from the motor side, and η represents the new coordinate on the motor side, defined by the transformation

$\eta = \theta - NK_s^{-1}\beta$. Here, β represents the desired impedance force, defined as $\beta = Z_{des}q$ with $Z_{des} = -K_q - D_q s$.

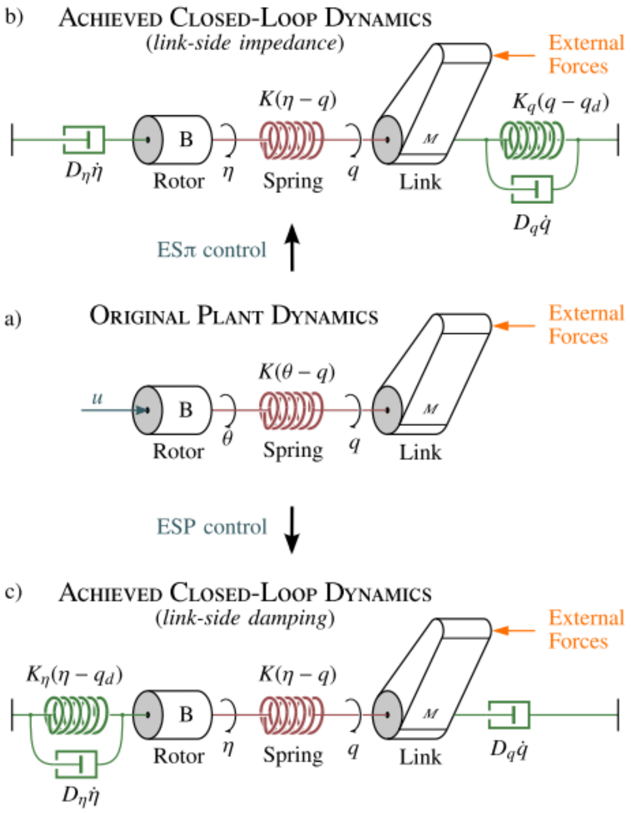
b)
ACHIEVED CLOSED-LOOP DYNAMICS
(link-side impedance)
External Forces
$K(\eta - q)$
$K_q(q - q_d)$
$D_\eta\dot{\eta}$
B
Rotor
η
Spring
q
Link
M
$D_q\dot{q}$
ESπ control
a)
ORIGINAL PLANT DYNAMICS
External Forces
$K(\theta - q)$
u
B
Rotor
θ
Spring
q
Link
M
ESP control
c)
ACHIEVED CLOSED-LOOP DYNAMICS
(link-side damping)
External Forces
$K_\eta(\eta - q_d)$
$K(\eta - q)$
B
Rotor
η
Spring
q
Link
M
$D_q\dot{q}$
$D_\eta\dot{\eta}$

Figure 2.6: (a) Graphical representation of a single linear-elastic joint (b) ESπ control achieves a full Impedance behavior directly on the link. (c) ESP control achieves damping directly on the link. [67]

2.3.4 Other Control

In addition to torque and impedance control, several methods can be applied to compliant actuators. Passivity-based control ensures stability by preserving system passivity [8, 68], while adaptive control with appropriate adaptation laws effectively stabilizes the system even with unmodeled behavior [69]. Controllers incorporating a disturbance observer (DoB) reject undesired disturbances, significantly enhancing robustness in both force controllers [58, 1, 70] and impedance controllers [63, 4, 71].

2.4 SEA Performance Evaluation

2.4.1 Performance under Force Control

In the context of force controllers, several indices have been proposed to evaluate actuator performance. Transmissibility is introduced to quantify how effectively motor force is transmitted to the load, compliance measures the reaction force with respect to an external force, and force sensitivity assesses how much spring force (i.e., spring deformation) is generated in response to an external force [42].

Additionally, to account for actuator limitations, such as maximum permissible velocity and maximum continuous motor torque, Chan proposed two new metrics: maximum torque transmissibility (MTT_τ) and maximum velocity transmissibility (MTT_v) in [72, 73]. These metrics represent the maximum torque transmissibility based on torque and velocity limitations, respectively. Furthermore, similar metrics can be derived to evaluate the maximum torque bandwidth, considering the constraints of τ and v.

2.4.2 Performance under Impedance Control

The performance of impedance control can be described using several metrics. In haptic devices, the Z-width is often used to represent the range of achievable impedance through frequency analysis [74]. To further assess performance, the Z-region, which combines Z-width and Z-depth, where Z-depth represents the achievable frequency range [4], provides a more comprehensive view by including both impedance and frequency considerations [4],[71], as shown in Fig. 2.7. Additionally, independent metrics like M-width, D-width, and K-width are used to describe the rendered mass, damping, and stiffness, respectively, allowing for a more detailed analysis of system dynamics [75].

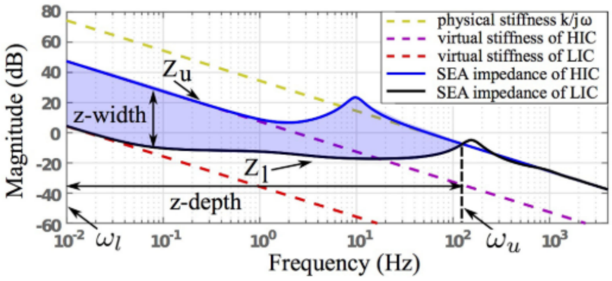

Figure 2.7: Z-region surrounded by the highest impedance controller (HIC) and the lowest impedance controller (LIC). This figure shows achievable SEA impedance ranges by modulating the gain scale GS =1 . The control gains are solved using the critically damped gain design criterion. [4]

3 Methodology and Analysis

SEA provides the torque source for robotic systems, and the impedance controller allows the user to define the desired impedance during interaction with the environment. One of the key control strategies is force cascaded impedance control (CIC), which achieves this by minimizing the error between desired and actual torque. On the other hand, elastic structure preserving impedance (ESPi) control is another strategy that can also provide the desired impedance in different approach.

In this chapter, the goal is to propose the concept of evaluation impedance-controlled SEA system through three featured perspectives, each examining a different performance metric. These perspectives are outlined in Fig. 3.1, providing an overview of the metrics and their relation to the applied controllers.

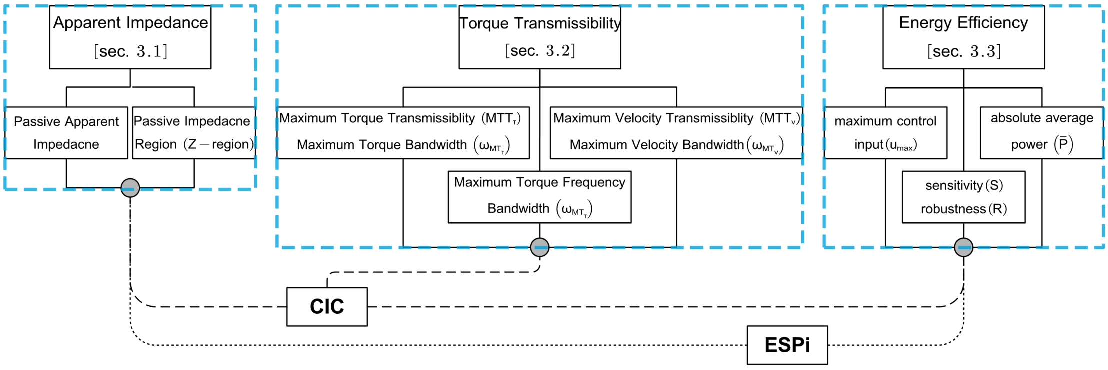
Apparent Impedance
[sec. 3.1]
Passive Apparent Impedacne
Passive Impedacne Region (Z − region)
Torque Transmissibility
[sec. 3.2]
Maximum Torque Transmissiblity (MTT$_\tau$)
Maximum Torque Bandwidth (ω_{MT_τ})
Maximum Velocity Transmissiblity (MTT$_v$)
Maximum Velocity Bandwidth (ω_{MT_v})
Maximum Torque Frequency Bandwidth (ω_{MT_f})
Energy Efficiency
[sec. 3.3]
maximum control input (u_{max})
absolute average power (P)
sensitivity (S)
robustness (R)
CIC
ESPi

Figure 3.1: Overview of the structure in Chapter 3. The dotted lines represent the relationships between the applied controllers and the metrics.

The first perspective focuses on the apparent passive impedance of impedance controlled SEA system, looking into how impedance control stiffness and torque control proportional gain influence system passivity and the achievable passive impedance region for both CIC and ESPi control in section 3.1.

However, the desired impedance force cannot always be fully transmitted through the controlled system due to actuator limitations specified in the datasheet. The second perspective examines the torque/velocity transmissibility of the CIC-controlled SEA, considering the nominal maximum continuous torque and permissible velocity. The evaluation results, defined by feasible frequency width and maximum torque generation constraints for achieving the full desired output torque, are presented in section 3.2[1].

Furthermore, robustness and energy efficiency under disturbances are crucial for overall robotic system design. The third perspective examines these metrics for both controllers using transfer functions, as discussed in section 3.3.

It is noticeable that all system and controller parameters used in the analysis throughout this thesis are listed in Table 3.1. Any non-identical parameters are specifically marked in the contents.

Table 3.1: Parameter Values

Parameter	**Value**	**Unit**	**Parameter**	**Value**	**Unit**
K_s	300	Nm/rad	N	1	–
B	0.05825	kg	K_p	3	–
M	1	kg	K_d	0.02	–
D_m	0.2	–	D_q	$2\sqrt{BK_q}$	–
D_l	1.1	–			

---

[1] It is worth noting that ESPi, as a feedback equivalence based controller [76], cannot be directly analyzed through force transmissibility.

3.1 Impedance Evaluation under Impedance Control

3.1.1 Controlled Apparent Impedance

Force Cascaded Impedance Control

In general, the impedance Z can be interpreted as the relationship between the system's response and the external force, typically defined as the ratio of output torque or external torque to the link's velocity or position, as shown in equation (2.5). Based on the definition of Z_{imp} with output torque, which defined as spring torque τ_s, the impedance at the spring port under the CIC framework, derived from equations (2.1) and (2.6), is given as,

$$Z^{CIC}_{spring}(s) = \frac{-\tau_s}{sq} = \frac{P_m^{-1}K_s - N^{-1}K_sC_fZ_{des}}{P_m^{-1} + N^{-2}K_s + N^{-1}K_sC_f}\frac{1}{s}, \tag{3.1}$$

As is well known, ensuring system stability is paramount. A necessary condition for stability is the passivity of the system. The passivity of the system can be defined by the following criteria (for detailed derivations, refer to [77]):

- The real part of the impedance should not be smaller than zero: $\mathfrak{Re}(Z) \geq 0$.
- The phase of the impedance should lie between $-90°$ and $90°$.

The real part of the CIC impedance at the spring port $\mathfrak{Re}(Z^{CIC}_{spring}(s))$ is given as,

$$\begin{aligned}\mathfrak{Re}(Z^{CIC}_{spring}(j\omega)) = {} & \frac{ND_mK_s\left(N^{-1}K_s - K_qK_p + KK_p\right)}{\left(ND_m\omega + K_sK_d\omega\right)^2 + \left(K_sK_p + N^{-1}K_s - NB\omega^2\right)^2} \\ & + \frac{NK_dK_s\left(BK_s\omega^2 - BK_q\omega^2 + K_qN^{-2}K_s\right)}{\left(ND_m\omega + K_sK_d\omega\right)^2 + \left(K_sK_p + N^{-1}K_s - NB\omega^2\right)^2},\end{aligned} \tag{3.2}$$

which is evaluated with $s = j\omega$.

Due to $\mathfrak{Re}(Z^{CIC}_{spring}(s)) \geq 0$, the passivity condition can be further simplified as,

$$\frac{K_q}{K_s} \leq 1 \implies K_s \geq K_q. \tag{3.3}$$

It is evident that in CIC there is an upper bound on the impedance control gain K_q, regardless of the torque controller coefficients (K_p, K_d). Under passivity conditions, the desired target impedance stiffness cannot exceed the physical stiffness K_s of the system. This implies that a high rendered stiffness would violate the passivity condition. However, this strict limitation on K_q can be relaxed if we evaluate the impedance including the load dynamics at the load port [78].

The port concept, illustrated as a circuit diagram in Fig. 3.2 introduced in [78], equates the mechanical system's inertia, damping, and spring to the circuit's inductance, resistance, and capacitance. The two ports, representing the spring and load, correspond to the observations at τ_s and τ_{ext}, highlighted in yellow in Fig. 3.2. The power observed from the two plants, P_m and P_l, is derived as the product of flow and effort, corresponding to the spring's ω_m and τ_s, and the load's ω_l and τ_l, respectively.

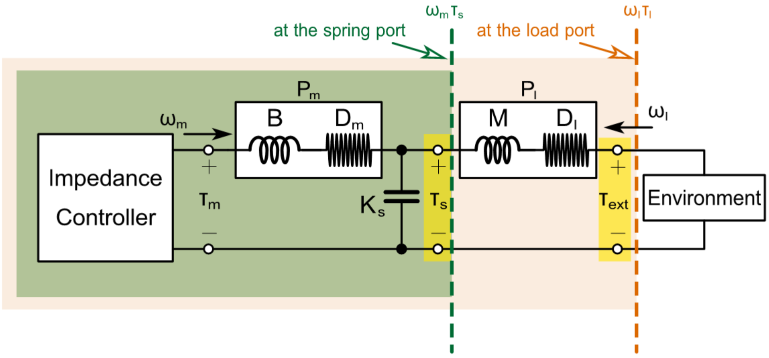

Figure 3.2: Port concept of the SEA system represented as a circuit. The green color corresponds to the spring port, the orange to the load port, and the outputs of both ports are highlighted in yellow.

Unlike Z_{spring} observed from τ_s, another way that presents the impedance at the load port, shortly Z_{load}, additive with the load dynamics P_l is given as,

$$Z_{load}(s) = Z_{spring}(s) + Ms + D_l. \tag{3.4}$$

where the damping D_l and the load inertia M explicitly represent P_l. Hence, the output of the overall system is treated as the external torque τ_{ext}.

In CIC framework, the real part of the impedance $\mathfrak{Re}(Z^{CIC}_{load}(j\omega))$ includes the additional D_l term compared to $\mathfrak{Re}(Z^{CIC}_{spring}(j\omega))$, which provides a margin for increasing the upper bound of K_q. This means that, under this definition, the rendered stiffness can exceed the physical stiffness. It is said to relax the conservatism of the passivity condition for impedance-controlled SEAs.

In order to validate the theory and analyze the apparent impedance in impedance controlled systems, we set the value of the parameters as shown in Table 3.1. We defined a new variable η_q as,

$$\eta_q = \frac{K_q}{K_s}. \tag{3.5}$$

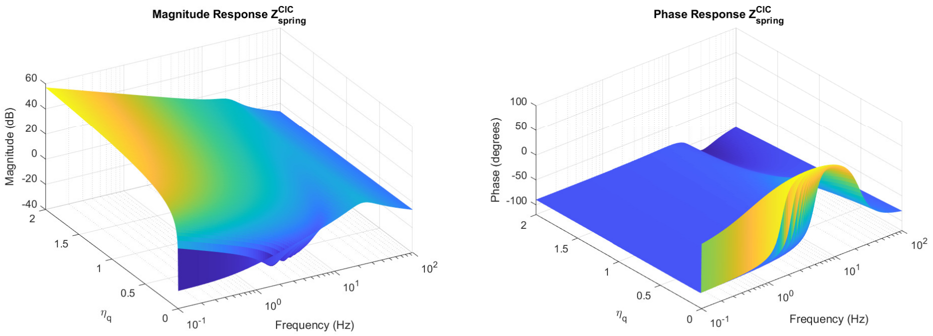

(a) Impedance at spring port with respect to η_q

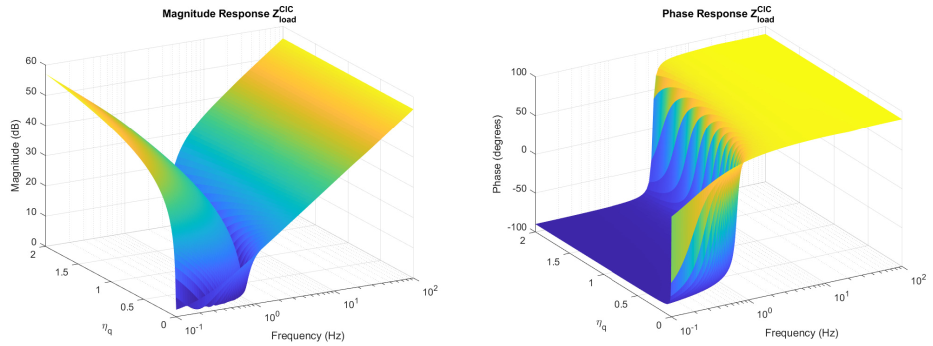

(b) Impedance at load port with respect to η_q

Figure 3.3: Comparison of apparent impedance at spring and load ports wrt. η_q under the CIC framework.

The impedance behavior under three different cases is discussed here, specifically the scenarios $\eta_q \leq 1$ and $\eta_q > 1$ at the spring port, and $\eta_q > 1$ at the load port. First, the overall tendency of impedance behavior corresponding to η_q changes is shown in

Fig. 3.3a and Fig. 3.3b. It is evident that, when considering the load dynamics, the magnitude response exhibits a fold at certain frequencies, and the phase response shows a significant rise from certain frequencies onward. Furthermore, these specific frequencies increase as η_q increases.

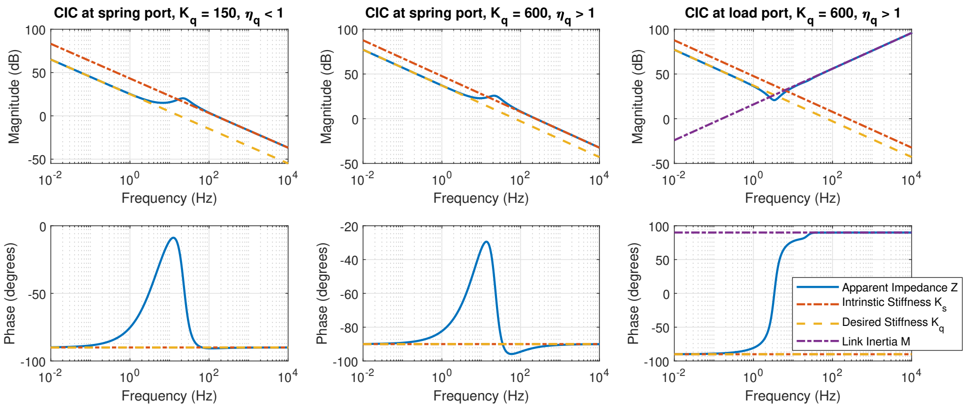

Figure 3.4: Apparent Impedance in CIC.$D_q = 2\sqrt{BK_q}$ has been selected for critically damped impedance. Three cases are evaluated: ($\eta_q < 1$) at the spring port, and ($\eta_q > 1$) evaluated at both the spring port and load port.

The apparent impedance evaluated at spring port shows frequency-variant characteristics dominated by K_q and K_p. The apparent impedance is dominated by K_q, referred to active impedance, in the low-frequency range, while in the high-frequency range, the intrinsic stiffness K_s, namely passive impedance, dominates, as shown in the first two columns of Fig. 3.4 highlighted by dashed and solid-line alignments, where K_s is assigned as half and twice the physical stiffness K_s, respectively, i.e $\eta_q \leq 1$ and $\eta_q > 1$. The apparent impedance evaluated at frequency (left and right) extremities provides convergences,

$$Z^{CIC}_{spring}|_{s\to 0} = K_q \left(\frac{K_p}{K_p + 1} \right), \tag{3.6}$$

$$Z^{CIC}_{spring}|_{s\to\infty} = K_s \left(1 + \frac{D_q K_d}{B} \right). \tag{3.7}$$

Equation (3.6) shows the stationary apparent impedance $\leq K_q$, approaching to K_q if K_p is sufficiently large. In contrast, the dynamical apparent impedance at right extremity in equation (3.12) $\geq K_s$. The motor inertia B scales down the effect from controlled damping D_q and K_d, thus preventing the alignment to intrinsic stiffness.

The passivity of controlled impedance has been violated where the phase margin clearly exceeds $-90°$, as shown in the second column from Fig. 3.4 for $\eta_q > 1$ case. However, the additional D_l evaluated for load port impedance in equation (3.4) provides a buffer for K_q, maintaining the phase within the passive region, illustrated in the third column of Fig. 3.4. Therefore, considering load dynamics allows K_q in desired impedance to exceed K_s compared to impedance at spring port.

The apparent impedance evaluated at load port converges to the load inertia M in the high-frequency domain while the impedance at low frequency has not been influenced by load dynamics among three selected cases in Fig. 3.4.

Elastic Structure Preserving Impedance Control

The apparent impedance controlled by ESPi is given as[2],

$$\begin{aligned} Z_{spring}^{ESPi}(s) &= \frac{-\tau_s}{sq} = -\frac{N^2P_m^{-1}(Z_{des}-K_s)+Z_{des}K_s}{N^2P_m^{-1}+K_s}\frac{1}{s} \\ &= \frac{N^2P_m^{-1}(K_q+K_s)+K_sK_q}{N^2P_m^{-1}+K_s}\frac{1}{s}+D_q \end{aligned} \tag{3.8}$$

Considering the passivity criterion for the system, the real part of the impedance at the spring port is given as,

$$\mathfrak{Re}(Z_{spring}^{ESPi}(j\omega)) = \frac{D_mN^{-2}K_s^2}{(D_m\omega)^2+(N^{-2}K-B\omega^2)^2}+D_q. \tag{3.9}$$

Obviously, $\mathfrak{Re}(Z_{spring}^{ESPi}(j\omega)) \geq 0, \quad \forall K_q, K_p, \omega$.

The passive impedance evaluated at the load port is referred to equation (3.4). Hence, the real part of the impedance at the load port is given as,

$$\mathfrak{Re}(Z_{load}^{ESPi}(j\omega)) = \frac{D_mN^{-2}K_s^2}{(D_m\omega)^2+(N^{-2}K-B\omega^2)^2}+D_q+D_l. \tag{3.10}$$

Apparently, the same conclusion for $\mathfrak{Re}(Z_{load}^{ESPi}(j\omega))$ will be derived as $\mathfrak{Re}(Z_{spring}^{ESPi}(j\omega))$.

The impedance behavior of ESPi controlled SEA exhibits a similar trend to that observed with CIC, with the exception occurring when K_q exceeds K_s as shown in Fig. 3.5[3]. The first two columns in Fig. 3.5 validate that the real part of

---

[2] Here, $\bar{u} = 0$ in τ_m, refer to equation(2.7)

[3] $D_q = 0$ has been applied.

Z_{spring}^{ESPi} does not impose any limitations on gain selection, even while adhering to the passivity.

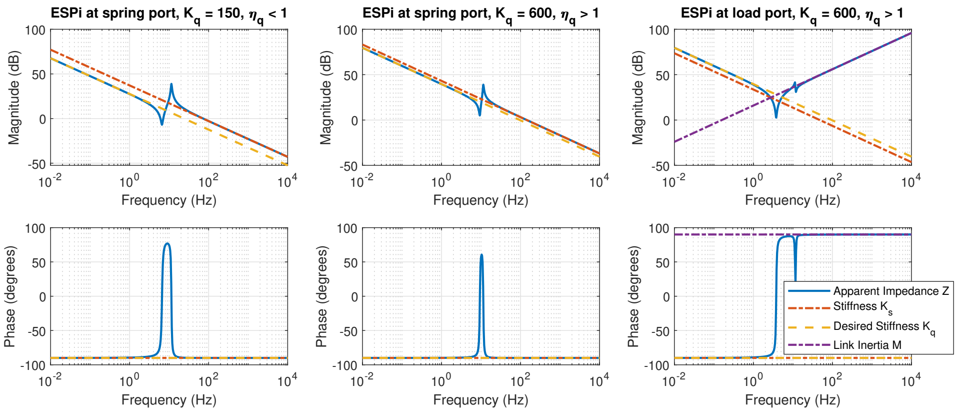

Figure 3.5: Apparent Impedance under the ESPi framework. The legend, D_q and three discussed cases condition are same as Fig. 3.4.

The apparent impedance evaluated at spring port at frequency extremities provides convergences,

$$Z_{spring}^{ESPi}|_{s\to 0} = K_q, \tag{3.11}$$

$$Z_{spring}^{ESPi}|_{s\to \infty} = K_s + K_q. \tag{3.12}$$

The impedance approaches to exactly K_q at low frequency, uninfluenced by any system parameters as impedance under CIC in (3.6). Meanwhile, the impedance converges to summation of the stiffness (gains) at high frequency, that differs from the CIC in (3.7).

3.1.2 Passive Impedance Region

This subsection introduces passive impedance region based on the foundation of the apparent impedance adhering to the passivity. The passive impedance region, referred as "Z-region" [4], is composed of two metrics: Z-width and Z-depth. Z-width represents the range of achievable impedance magnitude, a concept originally adopted in haptic devices [74], while Z-depth represents the achievable frequency range. The Z-region is defined as the area between the upper and lower boundaries of achievable impedance, Z_u and Z_l, over the frequency range between the upper and lower frequency limits, ω_u and ω_l,

$$\begin{aligned} Z_{region} &= \int_{\omega_l}^{\omega_u} W(\omega)\left|\log|Z_u(j\omega)| - \log|Z_l(j\omega)|\right| d\omega & (3.13) \\ &= \int_0^{\infty} W(\omega)\left|\log\frac{Z_u(j\omega)}{Z_l(j\omega)}\right| d\omega, & (3.14) \end{aligned}$$

where $W(\omega)$ is a weighting function that can account for specific performance requirements [4]. From here, $W(\omega) = 1$ has been assumed for easy manipulation.

Force Cascaded Impedance Control

In our case, we set the frequency range from 0 to ∞, where Z_l corresponds to the rendered impedance when $K_q = K_{min,q}^{imp} = 0$ and Z_u corresponds to the maximum passive stiffness for $K_{max,q}^{imp}$. This ensures a seamless design of target impedance with preserving the passivity.

First, focusing on the Z-region at the spring port without P_l, the result is illustrated in Fig. 3.6a under the assumption of a fixed torque controller gain.

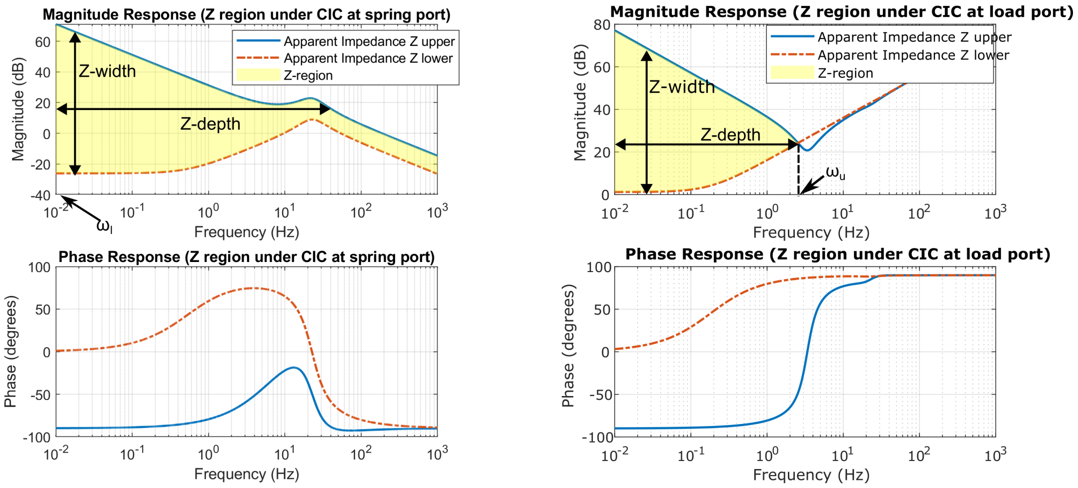

(a) Z-region at spring port (b) Z-region at load port

Figure 3.6: Comparison of Z-region at spring port (left) and load port (right) under CIC framework.

The maximum passive stiffness related to Z-region at the spring port is adopted as K_s from sec. 3.1.1. The Z-region spanned by Z_u^{CIC} and Z_l^{CIC} indicates the range of achievable impedance, illustrated in Fig. 3.6a. This visual representation provides insight into how CIC-impedance behaves within these limits. A correspondent user-case utilizing the Z-region will be provided later in section 4.1.

An example upper bound Z_{load}^{upper} composed of dynamical transition from K_q to K_s evaluated at load port with preserving passivity is visualized in Fig. 3.6b, where $K_q = 2K_s$ has been applied. The first intersection of Z_{load}^{upper} and Z_{load}^{lower} occurs around 2.5Hz while no intersection appears in the Z-region evaluated at the spring port, illustrated in Fig. 3.6a.

To increase versatility, the Z-region evaluated at the load port is extended to 3D by considering various K_p in the range $[0.1, 100]$, as shown in Fig. 3.7b. The passive impedance region slightly increases as K_p increases, clearly illustrated in 2D plot with four sets of K_p in Fig. 3.7a.

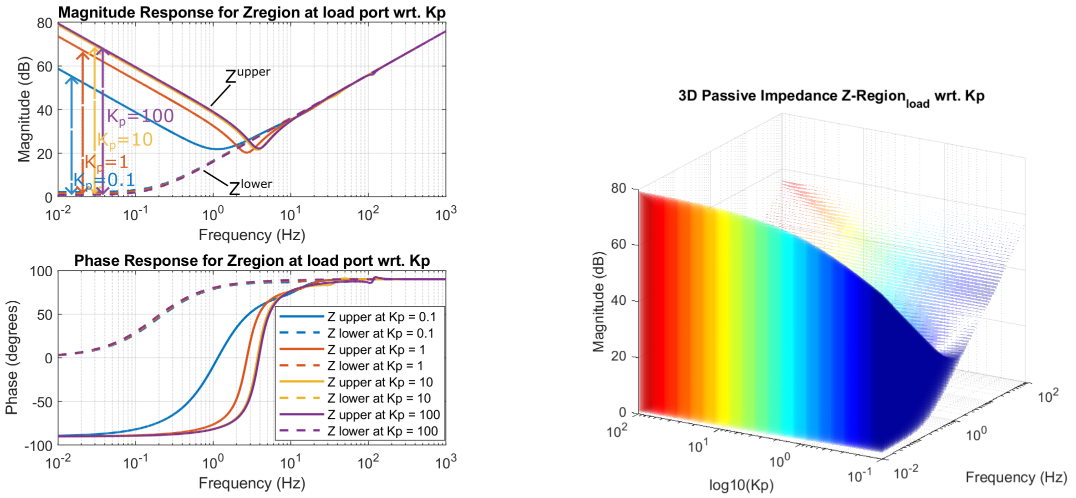

(a) Z-region with respect to K_p in a 2D view.

(b) Z-region with respect to K_p in a 3D view.

Figure 3.7: Comparison of Z-region Bode plots with respect to various K_p in 2D (a) and 3D (b) views.

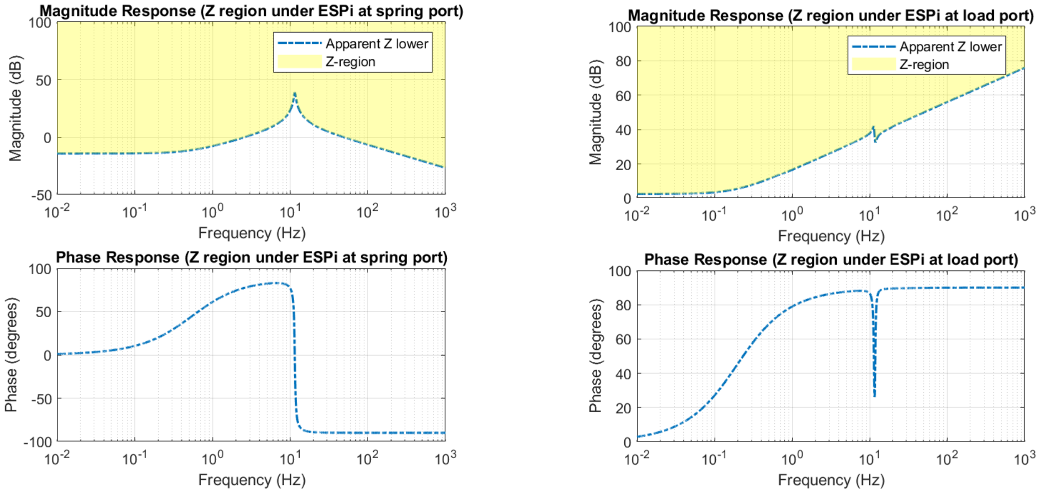

(a) Z-region evaluated at spring port (b) Z-region evaluated at load port

Figure 3.8: Comparison of Z-region at spring port (left) and load port (right) under ESPi framework.

Elasitc Structure Preserving Impedance Control

The passive impedance region under ESPi provides a much larger achievable impedance and frequency range since apparent passive impedance under ESPi has no constraint of K_q for preserving passivity theoretically in equation (3.10)[4], as shown in Fig. 3.8. This highlights the advantages of ESPi in terms of its extended flexibility in control parameters selection for maintaining passivity.

3.1.3 Summary

In subsection 3.1.1 and 3.1.2, it is concluded that CIC restricts the rendered stiffness to the physical stiffness conservatively and possesses the upper-and lower-bound constrained passive impedance region, mainly at low frequency. In contrast, ESPi controller imposes no limitations on rendered stiffness and achieves the larger passive impedance region, theoretically only constrained by lower-bound[5].

---

[4] $D_\eta = 0$ has been applied due to the derivation of equation (3.8).

[5] The derivation of CIC and ESPi is based on ideal assumptions, excluding factors such as friction, backlash, and actuator limitations, and utilizes frequency analysis. Additionally, the damping terms in the ESPi controller are neglected.

3.2 Force/Torque Transmissibility

In classical force control, force transmissibility quantifies the efficiency of transmitting motor force to the load side through the transmission (e.g., spring deformation in SEA) [42]. It is defined as,

$$T(s) = \frac{\tau_{out}}{\tau_m}, \tag{3.15}$$

However, large torque demands in SEA systems often lead to performance deterioration, known as the large force bandwidth problem (LFB) [72, 79, 80]. This occurs particularly at higher frequencies, where the transmitted torque is less than the theoretically desired value as the desired output approaches the system's maximum continuous motor torque[6], shortly $\tau_{mc,max}$. Chan et al. have proposed metrics to address this problem in classical force control; for details, refer to [73, 72].

To address the LFB problem effectively, it is essential to account for actuator limitations and understand how the control input τ_m influences the output torque τ_s, motor velocity $\dot{\theta}_m$, and link-side position q. For clarity, u is used to denote the control input, and ω_m represents the motor velocity in this subsection. From equation (2.1), these relationships are given as,

$$P_\tau(s) = \frac{\tau_s}{u} = \frac{N^{-1}P_m}{K_s^{-1} + P_l + N^{-2}P_m}, \tag{3.16}$$

$$P_{\omega_m}(s) = \frac{\omega_m}{u} = \frac{P_m\left(K_s^{-1} + P_l\right)s}{K_s^{-1} + P_l + N^{-2}P_m}, \tag{3.17}$$

$$P_q(s) = \frac{q}{u} = \frac{N^{-1}P_m P_l}{K_s^{-1} + P_l + N^{-2}P_m}, \tag{3.18}$$

where P_τ, P_{ω_m}, and P_q represent the transfer functions relating the control input u to the output torque, motor velocity, and link-side position, respectively.

3.2.1 Maximum Torque Transmissibility, Maximum Torque Bandwidth

To simplify the discussion of the actuator limitations, the integration of P_τ, P_{ω_m}, and P_q into the CIC block diagram is illustrated in Fig. 3.9. Two constraint equations for the ratio of the desired output torque τ_{des} to the control input u are given as,

---

[6] In general, it can be found in actuator datasheet.

Inner force tracking loop (i.e., orange loop):

$$u_{inn} = \frac{N^{-1}C_f}{1+N^{-1}C_f P_\tau}\tau_{des} = \frac{\big(1+K_s(P_l+N^{-2}P_m)\big)C_f N^{-1}}{1+K_s\big(P_l+N^{-2}P_m(1+C_f)\big)}\tau_{des}. \tag{3.19}$$

Outer position regulation loop (i.e., blue loop):

$$u_{out} = \frac{K_s^{-1}+P_l+N^{-2}P_m}{Z_{des}N^{-1}P_m P_l}\tau_{des}. \tag{3.20}$$

where u_{inn} and u_{out} denote the control inputs derived from the inner and outer loop control laws, respectively.

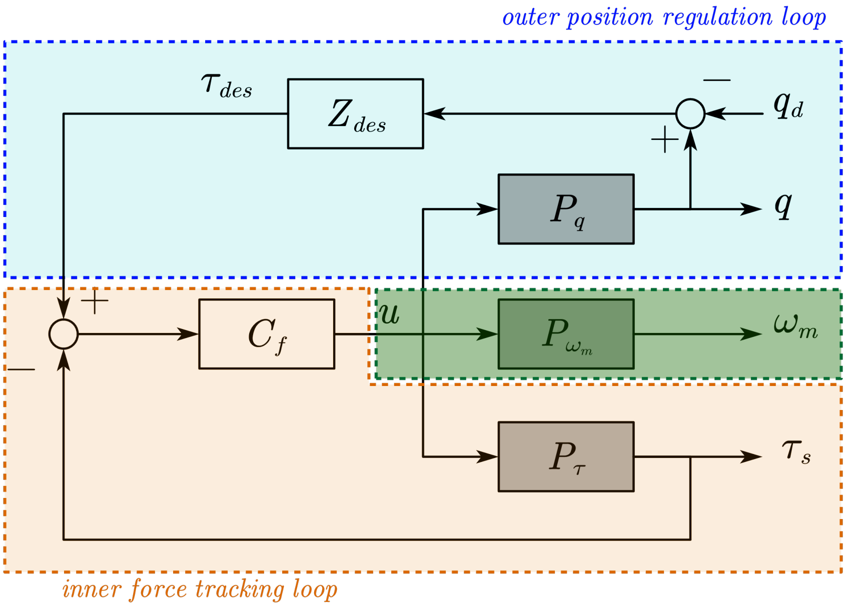
outer position regulation loop
τ_{des}
Z_{des}
$-$
q_d
$+$
P_q
q
$+$
u
C_f
P_{ω_m}
ω_m
$-$
P_τ
τ_s
inner force tracking loop

Figure 3.9: CIC block diagram with transfer function representations $(P_\tau, P_{\omega_m}, P_q)$, where the blue loop represents the outer position regulation loop, the orange loop represents the inner force tracking loop, and the green loop represents the relationship from u to ω_m.

To address the LFB problem, the maximum desired output torque, denoted as $\tau_{des,max}$, is expected to approach the maximum continuous motor torque $\tau_{mc,max}$.

When $\tau_{des} = \tau_{des,max}$ is pursued, the ratios between the control input u and $\tau_{des,max}$ are rearranged from equations (3.19) and (3.20) as

$$\frac{u_{inn}}{\tau_{des,max}} = \frac{\big(1 + K_s(P_l + N^{-2}P_m)\big)C_f N^{-1}}{1 + K_s(P_l + N^{-2}P_m(1 + C_f))}, \tag{3.21}$$

$$\frac{u_{out}}{\tau_{des,max}} = \frac{K_s^{-1} + P_l + N^{-2}P_m}{Z_{des}N^{-1}P_m P_l}. \tag{3.22}$$

From Fig. 2.4, the gear ratio amplifies the motor torque that

$$\tau_{des,max} = N\tau_{mc,max} \quad \Rightarrow \quad \tau_{mc,max} = N^{-1}\tau_{des,max}. \tag{3.23}$$

The maximum torque transmissibility, denoted as MTT_τ, is defined as,

$$MTT_\tau(s) = \frac{|u(s)|}{\tau_{mc,max}}, \tag{3.24}$$

which serves as a metric to tackle the LFB problem.

Based on (3.24), inserting (3.23) into the constraint equations (3.21) and (3.22), the MTT_τ for the inner and outer loop paths are derived as,

$$MTT_\tau^{inn}(s) = \frac{u_{inn}}{\tau_{des,max}} = \left|\frac{(1 + K_s(P_l + N^{-2}P_m))C_f}{1 + K_s(P_l + N^{-2}P_m(1 + C_f))}\right|, \tag{3.25}$$

$$MTT_\tau^{out}(s) = \frac{u_{out}}{\tau_{des,max}} = \left|\frac{N(K_s^{-1} + P_l + N^{-2}P_m)}{Z_{des}N^{-1}P_m P_l}\right|. \tag{3.26}$$

If MTT_τ greater 1 (0 dB) at any location over an interested frequency range, the control input u becomes insufficient to achieve the desired output torque τ_{des}, implying the actuator cannot deliver the full $\tau_{des,max}$. Therefore, to ensure large torque generation, MTT_τ must satisfy

$$MTT_\tau(s) \leq 1. \tag{3.27}$$

The maximum torque bandwidth, denoted as ω_{MT_τ}, is defined as the upper frequency limit guaranteeing maximum torque generation. This concept was first introduced for classical torque control in [72]. Since the CIC-controlled system involves two loops in Fig. 3.9, $\omega_{MT_\tau}^{CIC}$ is defined as,

$$\omega_{MT_\tau}^{CIC} = \min(\omega_{MT_\tau}^{inn}, \omega_{MT_\tau}^{out}), \tag{3.28}$$

where

$$\omega_{MT_\tau}^{out} = \arg\min_{\omega} \left\{\omega : MTT_\tau^{out}(j\omega) = 1\right\}, \tag{3.29}$$

and

$$\omega_{MT_\tau}^{inn} = \begin{cases} \arg\min_{\omega > \omega_{MT_\tau}^{inn,lower}} \left\{\omega : MTT_\tau^{inn}(j\omega) = 1\right\}, & \text{if } \omega_{MT_\tau}^{inn,lower} \text{ is defined,} \\ \arg\min_{\omega} \left\{\omega : MTT_\tau^{inn}(j\omega) = 1\right\}, & \text{otherwise.} \end{cases} \tag{3.30}$$

where

$$\omega_{MT_\tau}^{inn,lower} = \begin{cases} \arg\min_{\omega} \left\{\omega : MTT_\tau^{inn}(j\omega) = 1\right\}, & \text{if } MTT_\tau^{inn}(j\omega) > 0 \text{ as } \omega \to 0, \\ \text{undefined,} & \text{otherwise.} \end{cases} \tag{3.31}$$

Here, $s = j\omega$ is applied and $\omega_{MT_\tau}^{inn,lower}$ represents the lower frequency limit at which maximum torque generation is guaranteed and solely appears in the inner control loop.

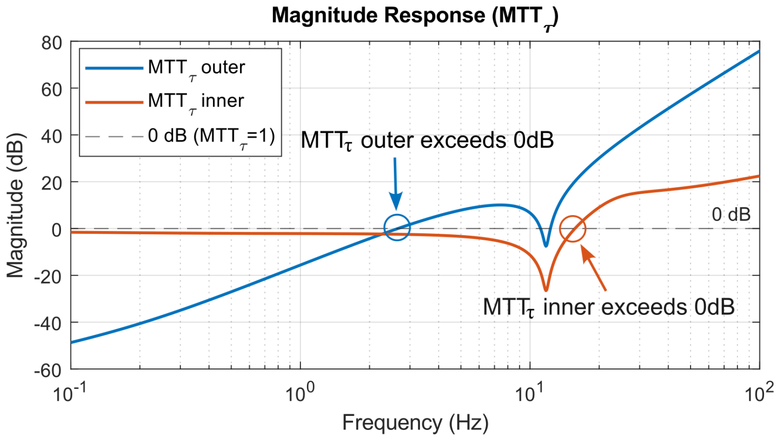

Figure 3.10: MTT_τ Bode plot with desired impedance $K_q = 250$, $D_q = 2\sqrt{BK_q}$.

Noticeably, equations (3.25) and (3.26) depend solely on K_p and K_q, which correspond to the inner and outer control loop, respectively. Besides, ω_{LFB} is introduced as a measure, representing a feasible width in frequency that ensures generation of τ_{des}^{max}. This facilitates comparative experiments to determine and validate the optimal gain (K_p or K_q) in CIC. These experiments are conducted in three cases:

1. specific K_q and K_p values
2. various K_q values for MTT_τ^{out}
3. various K_p values for MTT_τ^{inn}

Case1 with specific K_q and K_p.

The maximum torque bandwidth $\omega_{MT_\tau}^{CIC}$ is dominated by $\omega_{MT_\tau}^{out}$, as MTT_τ^{out} exceeds 0 dB at approximately 2.7 Hz, earlier than $\omega_{MT_\tau}^{inn}$, shown in Fig. 3.10. Furthermore, MTT_τ for both the inner and outer loops generally increases with frequency, indicating that the bandwidth preserving large torque generation is constrained to lower frequency ranges.

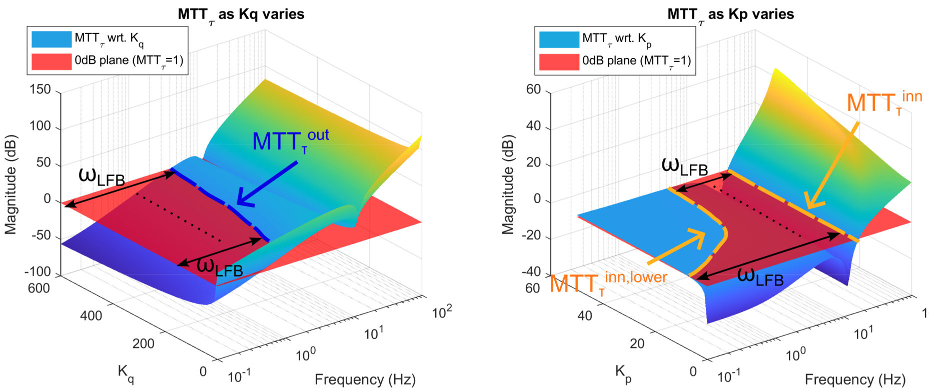

(a) (b)

Figure 3.11: MTT_τ Bode plot with respect to (a) variable K_q and (b) variable K_p. The red plane represents 0 dB plane. The colorful surface represents the MTT_τ. Here, $K_q = 250$ and $K_p = 3$ are applied.

Case2 with various K_q

According to equation (3.27), the controlled system should operate in the region ω_{LFB} where the MTT_τ surface lies below the 0 dB plane (i.e., the red plane) in Fig. 3.11a (3D view), corresponding directly to the red area in Fig. 3.12a(2D view).

The $\omega_{MT_\tau}^{out}$ trajectory as a function of K_q in (3.29) corresponds to the first intersection boundary between the two planes. The value of ω_{MT_τ} increases with K_q, indicating that a higher rendered stiffness (i.e., stiffer impedance) enables the actuator to deliver $\tau_{des,max}$, even at high frequencies.

Case3 with various K_p

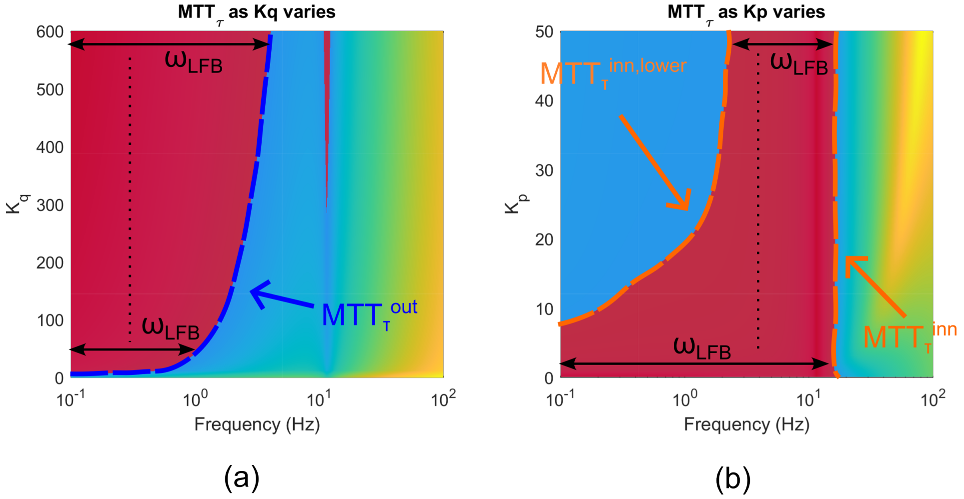

Figure 3.12: 2D MTT_τ Bode plot with respect to variable K_q and K_p from Fig. 3.11.

The same way is followed for finding ω_{LFB} in this case, which is constrained by $\omega_{MT_\tau}^{inn}$ and $\omega_{MT_\tau}^{inn,lower}$ trajectories from left and right side, respectively, as shown in Fig. 3.11b. The K_p range from 0.1 to 7.2 provides the largest ω_{LFB}, as marked in Fig. 3.12b, due to the absence of lower frequency limit and constant $\omega_{MT_\tau}^{inn}$ regardless of K_p. When K_p exceeds 7.2, $\omega_{MT_\tau}^{inn,lower}$ increases with K_p, leading to a reduction in ω_{LFB}. Therefore, selecting K_p within a smaller range is preferable to maximize ω_{LFB} and ensure the generation of the maximum desired output torque τ_{des}^{max}.

The intrinsic stiffness K_s and the gear ratio N have impact on MTT_τ. However, in this section, they are kept constant as the focus is on the selection of controller parameters[7]. For more details on the parameter selection of K_s and N in classical force control, refer to [72].

3.2.2 Maximum Velocity Transmissibility, Maximum Velocity Bandwidth

The maximum permissible motor velocity, denoted as $\omega_{m,per}$, limits the actuator's ability to achieve the desired output torque τ_{des}. The relationship describing how the motor velocity ω_m behaves under the desired output torque τ_{des}, constrained by the control input u, as derived from Fig. 3.9, is given as,

---

[7] While all system parameters influence the metrics according to the equations, in this analysis, only the control parameters are varied, and all other parameters are kept constant, as shown in Table 3.1.

Inner force tracking loop (i.e., orange + green loop):

$$\omega_m = P_{\omega_m} u_{inn} = P_{\omega_m} \frac{N^{-1} C_f}{1 + N^{-1} C_f P_\tau} \tau_{des}, \tag{3.32}$$

Outer position regulation loop (i.e., blue + green loop):

$$\omega_m = P_{\omega_m} u_{out} = P_{\omega_m} \frac{K_s^{-1} + P_l + N^{-2} P_m}{Z_{des} N^{-1} P_m P_l} \tau_{des}. \tag{3.33}$$

According to the definitions and constraints of MTT_τ in equations (3.24) and (3.27), the maximum velocity transmissibility, denoted as MTT_ω, is defined as,

$$MTT_\omega = \frac{|\omega_m|}{\omega_{m,per}} \leq 1, \tag{3.34}$$

which serves as a metric to address the LFB problem in terms of velocity limitations.

When $\tau_{des} = \tau_{des,max}$ is pursued, inserting equations (3.23) and (3.34) into the two constraints on ω_m in equations (3.32) and (3.33), the $MTT_\omega(s)$ for the inner and outer loop paths are derived as,

$$MTT_\omega^{inn}(s) = \left| \frac{C_f P_m (K_s^{-1} + P_l) s}{K_s^{-1} + P_l + N^{-2} P_m (1 + C_f)} \right| \frac{\tau_{m,cont}^{max}}{\omega_{m,per}}, \tag{3.35}$$

$$MTT_\omega^{out}(s) = \left| \frac{N P_m (K_s^{-1} + P_l) s}{Z_{des} N^{-1} P_m P_l} \right| \frac{\tau_{m,cont}^{max}}{\omega_{m,per}}. \tag{3.36}$$

The maximum velocity bandwidth, ω_{MT_ω}, analogous to the definition of ω_{MT_τ} in equation (3.28), is defined as the upper frequency limit ensuring maximum output torque generation. It is given as,

$$\omega_{MT_\omega} = \min(\omega_{MT_\omega}^{inn}, \omega_{MT_\omega}^{out}), \tag{3.37}$$

where

$$\omega_{MT_\omega}^{out} = \arg\min_\omega \left\{ \omega : MTT_\omega^{out}(j\omega) = 1 \right\}, \tag{3.38}$$

and

$$\omega_{MT_\omega}^{inn} = \begin{cases} \arg\min_{\omega > \omega_{MT_\omega}^{inn,lower}} \left\{ \omega : MTT_\omega^{inn}(j\omega) = 1 \right\}, & \text{if } \omega_{MT_\omega}^{inn,lower} \text{ is defined,} \\ \arg\min_\omega \left\{ \omega : MTT_\omega^{inn}(j\omega) = 1 \right\}, & \text{otherwise,} \end{cases} \tag{3.39}$$

where

$$\omega_{MT_\omega}^{inn,lower} = \begin{cases} \arg\min_\omega \left\{ \omega : MTT_\omega^{inn}(j\omega) = 1 \right\}, & \text{if } MTT_\omega^{inn}(j\omega) > 0 \text{ as } \omega \to 0, \\ \text{undefined}, & \text{otherwise.} \end{cases} \tag{3.40}$$

Here, $\omega_{MT_\omega}^{inn}$ and $\omega_{MT_\omega}^{out}$ represent the upper frequency limits derived from the inner and outer loops, respectively, while $\omega_{MT_\omega}^{inn,lower}$ represents the lower frequency limit derived from the inner loop. These definitions are analogous to $\omega_{MT_\tau}^{inn}$, $\omega_{MT_\tau}^{out}$, and $\omega_{MT_\tau}^{inn,lower}$ in equations (3.30), (3.29), and (3.31).

A new variable, $\eta_{\tau,\omega}$, is introduced to represent the ratio of the maximum continuous motor torque to the maximum permissible velocity. It is defined as,

$$\eta_{\tau,\omega} = \frac{\tau_{mc,max}}{\omega_{m,per}}. \tag{3.41}$$

Equations (3.35) and (3.36) can be reformulated in terms of $\eta_{\tau,\omega}$ as,

$$MTT_\omega^{inn} = \left| \frac{C_f P_m (K^{-1} + P_l) s}{K^{-1} + P_l + N^{-2} P_m (1 + C_f)} \right| \eta_{\tau,\omega}, \tag{3.42}$$

$$MTT_\omega^{out} = \left| \frac{N P_m (K^{-1} + P_l) s}{Z_{des} N^{-1} P_m P_l} \right| \eta_{\tau,\omega}. \tag{3.43}$$

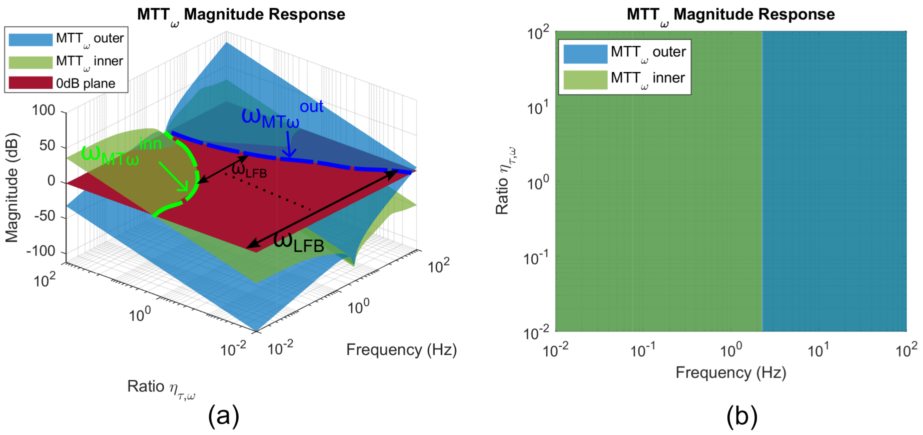

Figure 3.13: MTT_ω Bode plot with respect to variable $\eta_{\tau,\omega}$. Here, $K_p = 3$ and $K_q = 250$ are applied.

To understand the effects of $\eta_{\tau,\omega}$ on the feasible frequency width ω_{LFB}, three different cases will be analyzed:

1. specific K_q, K_p, and varying $\eta_{\tau,\omega}$
2. specific K_q, and varying $\eta_{\tau,\omega}$, K_p
3. specific K_p, and varying $\eta_{\tau,\omega}$, K_q

Case1 with specific K_q*,* K_p*, and varying* $\eta_{\tau,\omega}$

MTT_{ω}^{inn} dominates at low frequencies, while MTT_{ω}^{out} dominates at high frequencies, with a critical frequency of 2.3 Hz that remains independent of $\eta_{\tau,\omega}$, as shown in Fig. 3.13b. Based on the chosen control parameters, $\omega_{MT_{\omega}}^{out}$ consistently dominates $\omega_{MT_{\omega}}$ in equation (3.37), as illustrated in Fig. 3.13a. Notably, increasing $\eta_{\tau,\omega}$ decreases $\omega_{MT_{\omega}}^{out}$ and $\omega_{MT_{\omega}}^{inn,lower}$ is defined when $\eta_{\tau,\omega} > 1.2$, which leads to the reduced feasible frequency width ω_{LFB}.

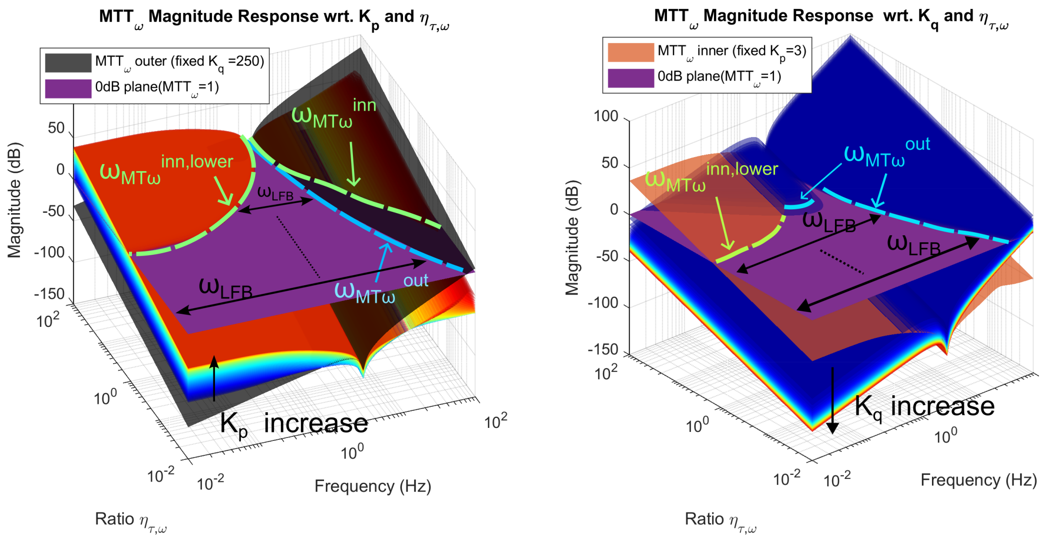

(a) MTT_{ω} wrt. $\eta_{\tau,\omega}$ and K_p

(b) MTT_{ω} wrt. $\eta_{\tau,\omega}$ and K_q

Figure 3.14: MTT_{ω} wrt. $\eta_{\tau,\omega}$ and K_p(left) or K_q(right), From the blue color to red color represent the value from low to high.

Case2 with specific K_q*, and varying* $\eta_{\tau,\omega}$*,* K_p

Once K_p grows, $\omega_{MT_{\omega}}^{inn,lower}$ decreases, exhibiting the same trend as $\omega_{MT_{\tau}}^{inn,lower}$ mentioned in subsection 3.2.1, as shown in Fig. 3.14a. Even though $\omega_{MT_{\omega}}^{out}$ increases with K_q (i.e, validation shows in Case 3), $\omega_{MT_{\omega}}^{out}$ remains smaller than $\omega_{MT_{\omega}}^{inn,lower}$, where $\omega_{MT_{\omega}}^{out}$ illustrated in Fig. 3.14a is derived from large K_q. This indicates that ω_{MT_ω} is primarily dominated by $\omega^{out}_{MT_\omega}$. Additionally, ω_{LFB} decreases with increasing $\eta_{\tau,\omega}$, which verifying the Case1 conclusion.

Case3 with specific K_p, and varying $\eta_{\tau,\omega}$, K_q

$\omega^{out}_{MT_\tau}$ rises with K_q, exhibiting an expansion of the feasible frequency width ω_{LFB} under fixed $\eta_{\tau,\omega}$, as shown in Fig. 3.14b. Remarkably, $\omega^{out}_{MT_\tau}$ decreases as $\eta_{\tau,\omega}$ growing and it has a discontinuity at $\eta_{\tau,\omega}$ equal 4.6, representing that the ω_{LFB} reduces with the increase of $\eta_{\tau,\omega}$, which verifying the Case1 conclusion.

The gear ratio N and the intrinsic stiffness K_s play an important role on ω_{MT_ω}. However, in this subsection, they are kept constant since our focus is on the selection of controller parameters. For more details on the effect of N and K_s, refer to [73].

3.2.3 Maximum Torque Frequency Bandwidth

The two actuator limitations, $\tau_{mc,max}$ and $\omega_{m,per}$, both hinder the actuator transmissibility and define their own frequency boundaries, ω_{MT_τ} and ω_{MT_ω}, respectively. To guarantee large torque generation, it is necessary to adhere to these boundaries by choosing the minimum as the maximum torque frequency bandwidth [72],

$$\omega_{MT} = \min(\omega_{MT_\tau}, \omega_{MT_\omega}) \tag{3.44}$$

Besides, CIC introduces the lower frequency boundary in (3.31) and (3.40), resulting in the maximum torque frequency bandwidth lower frequency boundary, denoted as ω^{lower}_{MT}. It is defined as,

$$\omega^{lower}_{MT} = \min(\omega^{inn,lower}_{MT_\tau}, \omega^{inn,lower}_{MT_\omega}) \tag{3.45}$$

For the user-case in section 4.2, it is necessary to discuss the frequency ranges where ω_{MT_τ} dominates versus where ω_{MT_ω} is primary. The case with fixed K_q and K_p will be discussed.

Equations (3.25) and (3.26) show that ω_{MT_τ} is independent of $\eta_{\tau,\omega}$. The first intersection of the blue area and the red area, ω_{MT_τ}, has a constant frequency of 2.7 Hz, as illustrated in Fig. 3.15, which matches observations in subsection 3.2.1 Case1. In comparison, the intersection of the green area and the red area, ω_{MT_ω}, which indicates as the lower frequency limit of the ω^{lower}_{MT}, grows with $\eta_{\tau,\omega}$, particularly for $\eta_{\tau,\omega}$ greater than 1.8. Noticeably, the feasible frequency width ω_{LFB} narrows as $\eta_{\tau,\omega}$ rises beyond 1.8, and when $\eta_{\tau,\omega}$ reaches 30.8, ω_{LFB} vanishes.

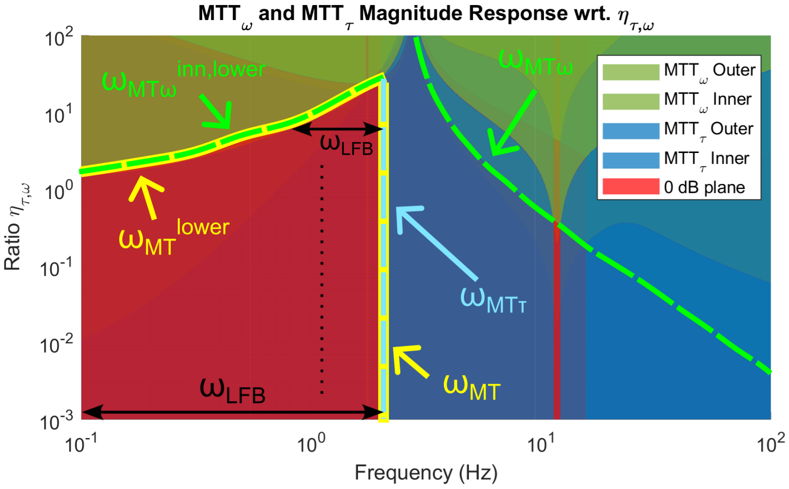

Figure 3.15: ω_{MT} Bode plot with MTT_ω represented in green, MTT_τ in blue, and the 0 dB plane in red. Here, $K_q = 250$, $D_q = 2\sqrt{BK_q}$ and $K_p = 3$ are applied.

From this analysis, it can be concluded that selecting a larger $\tau_{mc,max}$ or a smaller $\omega_{m,per}$ is preferable for maximizing the feasible frequency width for maximum torque generation.

3.3 Energy Efficiency under Disturbance

The previous subsection introduced metrics covers the fidelity control on achievable impedance and force, it is also crucial to evaluate robustness of controlled SEA. Sensitivity and robustness are metrics used to quantify the controller's relationship with respect to τ_{ext}.

The sensitivity $S(s)$ of a SEA is defined as the extent of spring deformations responds to external forces/torques [42],

$$S(s) = \frac{\theta - q}{\tau_{ext}} = \frac{\Delta x_s}{\tau_{ext}}. \tag{3.46}$$

The robustness $R(s)$ describes how the controlled system preserve performance under disturbance[1, 81], namely,

$$R(s) = \frac{\tau_m}{\tau_{ext}} \tag{3.47}$$

Besides, energy efficiency is significant for design of controlled SEA. It is often discussed how the choice of controller or the selection of elasticity in an elastic system can minimize the overall mechanical power consumption associated with the desired motion [82]. Generally, four classes of power consumption are defined, as introduced in [83]: net power, absolute power, positive-only power, and generalized power. In robotics and bipedal biomechanics, absolute power is widely used for analysis,

$$\bar{P} = \frac{1}{T}\int_0^T \mid P(t) \mid dt \tag{3.48}$$

which is selected as one of interested metrics and utilized throughout this subsection.

3.3.1 Force Cascaded Impedance Control

To simplify the discussion, the CIC block diagram, incorporating the transfer functions P_q, P_τ, and P_d, which are independent of any controllers, is shown in Fig. 3.16. Additionally, P_d represents the ratio between the disturbance τ_{ext} and the link position q, which is given as,

$$P_d = \frac{q}{\tau_{ext}} = \frac{P_m^{-1} + N^{-2}K}{P_m^{-1}P_l^{-1} + K(N^{-2}P_l^{-1} + P_m^{-1})}. \tag{3.49}$$

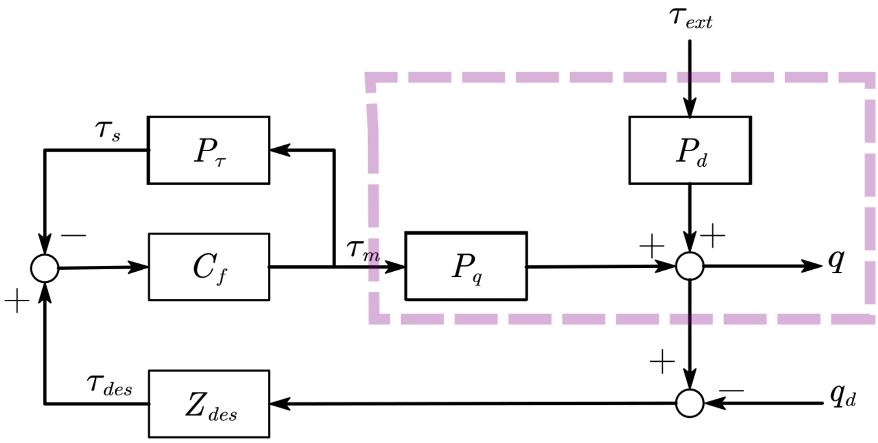

Figure 3.16: CIC diagram with transfer function P_q, P_τ, and P_d

where P_q and P_τ have been defined in (3.18) and (3.16), respectively.

Together with feed-forward dynamics of P_q, the output q is affected by two force-ports,

$$q = P_q\tau_m + P_d\tau_{ext}. \tag{3.50}$$

as shown in the purple dashed bounded box in Fig. 3.16.

Several transfer functions, essential for energy efficiency and robustness in CIC-controlled SEA, are derived from equations (2.6), (2.1), and (3.16). These are given by,

$$G_u^{CIC} = \frac{\tau_m}{\tau_{ext}} = \frac{Z_{des}C_fP_d}{1 + C_f(P_\tau - P_qZ_{des})}, \tag{3.51}$$

$$G_\theta^{CIC} = \frac{\theta}{\tau_{ext}} = \frac{C_fZ_{des} + N^{-1}K_s + K_sC_f}{P_m^{-1}P_l^{-1} + K_s(N^{-2}P_l^{-1} + P_m^{-1}) + N^{-1}K_sC_f(P_l^{-1} - Z_{des})}, \tag{3.52}$$

$$G_{\dot\theta}^{CIC} = \frac{\dot\theta}{\tau_{ext}} = sG_\theta^{CIC}, \tag{3.53}$$

where G_u^{CIC}, G_θ^{CIC}, and $G_{\dot\theta}^{CIC}$ represent the transfer functions relating the control input, motor-side position, and motor velocity to external torque, respectively.

The robustness and sensitivity are selected by definition of (3.47) and (3.46). Thus, $R(s)^{CIC}$ equals (3.51). S is given as,

$$S(s)^{CIC} = G_\theta^{CIC} - P_d. \tag{3.54}$$

Correspondingly, the absolute power is updated based on equations (3.51) and (3.53), along with the fact that the product of effort u and flow $\dot{\theta}$ represents the exerted power,

$$\bar{P}^{CIC} = \frac{1}{T}\int_0^T \mid G_u^{CIC} G_\theta^{CIC} \tau_{ext}^2 \mid dt. \tag{3.55}$$

This describes a case where the goal is to maintain the output at an equilibrium position. When a disturbance occurs, such as an impact torque or periodic torque, the controller requires to exert a specific amount of mechanical energy to achieve the desired impedance behavior and maintain the equilibrium.

3.3.2 Elastic structure Preserving Impedance Control

The ESPi related derivation reused the components from CIC. The control input τ_m based on equations (2.7) and the coordinate transformation[8] introduced in [10] is given as ,

$$\tau_m = Y_q q + Y_\tau \tau_{ext} - Y_r q_d, \tag{3.56}$$

where Y_q, Y_τ, and Y_r are given as,

$$\begin{aligned} Y_q &= \frac{N(Z_{des}(P_m^{-1} + N^{-2}K_s + D_\eta s) - D_\eta(P_l^{-1} + K_s)s)}{K_s} \\ Y_\tau &= \frac{ND_\eta s}{K_s} \\ Y_r &= \frac{NZ_{des}(P_m^{-1} + N^{-2}K_s + D_\eta s)}{K_s} \end{aligned} \tag{3.57}$$

which is highlighted by orange box in Fig. 3.17 (cf. Fig. 3.16). Y_q and Y_r represents the negative coefficients due to their sign definitions.

Notably, transfer functions denoted by capital P represent relationships derived from the original SEA system, independent of any controllers. Transfer functions denoted by capital Y correspond to relationships involving the control input τ_m. Transfer functions denoted by capital G represent relationships derived from the controlled SEA system, which are strongly dependent on the controllers.

Transfer functions essential for the discussion of energy efficiency and robustness in ESPi-controlled SEA are derived from equations (2.1), (2.7), and (3.50). These

---

[8] Here, the transformation $\beta = Z_{des}(q - q_d)$ and $Z_{des} = -K_q - D_q s$ are used.

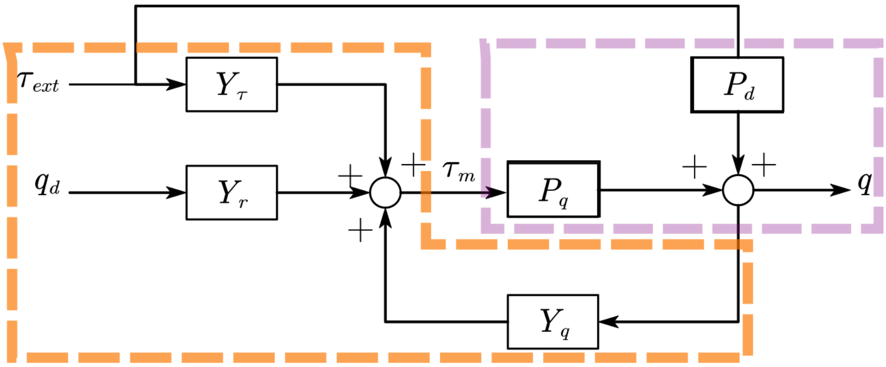

Figure 3.17: ESPi control diagram with transfer functions P_q, P_d, Y_q, Y_r, and Y_τ.

transfer functions are expressed as,

$$G_u^{ESPi} = \frac{\tau_m}{\tau_{ext}} = \frac{Y_q P_d + Y_\tau}{1 - Y_q P_q}, \tag{3.58}$$

$$G_\theta^{ESPi} = \frac{\theta}{\tau_{ext}} = \frac{(P_l^{-1} + K_s)Y_\tau + (Y_q + N^{-1}K_s)}{P_m^{-1}P_l^{-1} + K_s(N^{-2}P_l^{-1} + P_m^{-1}) - N^{-1}K_s Y_q}, \tag{3.59}$$

$$G_{\dot\theta}^{ESPi} = \frac{\dot\theta}{\tau_{ext}} = sG_\theta^{ESPi}, \tag{3.60}$$

where G_u^{ESPi}, G_θ^{ESPi}, and $G_{\dot\theta}^{ESPi}$ represent the transfer functions relating the control input, motor-side position, and motor velocity to external torque, respectively.

The robustness R and sensitivity S in ESPi-controlled SEA are derived as the same way for CIC-controlled SEA. Hence, $R(s)^{ESPi}$ equals (3.58) and S is expressed as,

$$S(s)^{ESPi} = G_\theta^{ESPi} - P_d. \tag{3.61}$$

Correspondingly, the absolute power is expressed as,

$$\bar{P}^{ESPi} = \frac{1}{T}\int_0^T \mid G_u^{ESPi} G_\theta^{ESPi} \tau_{ext}^2 \mid dt, \tag{3.62}$$

which has a similar formulation as CIC-controlled SEA in (3.55).

3.3.3 Transfer Functions related to Disturbance

In the previous subsection, several transfer functions related to τ_{ext} were introduced. To achieve an energy-efficient controlled SEA, a comparison of G_u and $G_{\dot\theta}$ between two different controllers for the case with specific Z_{des} and varying K_q are discussed below[9].

Case 1 with specific Z_{des}

The anti-resonance of G_u, shortly ω_{anti,G_u}, where τ_{ext} minimally affects τ_m under the same external torque, is identical for both controllers, with $\omega_{anti,G_u} = \sqrt{K/B}$ as in equations (3.51) and (3.58). This corresponds to the natural frequency of the uncontrolled SEA, denoted as ω_n, and is shown by the solid lines in Fig. 3.18. Moreover, with the anti-resonance power of four in G_u^{ESPi}, higher than that in G_u^{CIC}, the anti-peak of G_u^{ESPi} is deeper than that of G_u^{CIC}.

In contrast, the resonance of G_u, denoted as ω_{r,G_u}, where even a small external torque significantly affects the control input τ_m, shows no distinct differences between controllers, as seen in Fig. 3.18. However, in ESPi control, the effect of τ_{ext} on τ_m increases at high frequencies, particularly beyond ω_{anti,G_u}, indicating a theoretically high resonance. In CIC, this influence remains minimal due to the lack of a pronounced peak at ω_{r,G_u}.

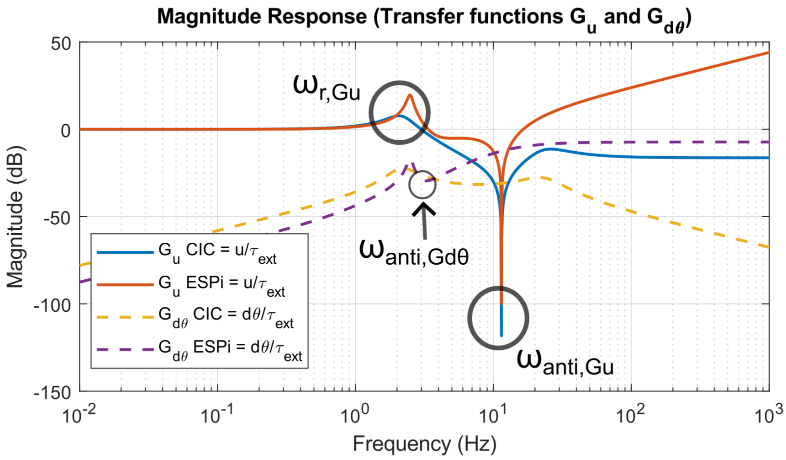

Figure 3.18: transfer functions comparison with desired impedance $K_q = 250$, $D_q = 2\sqrt{BK_q}$. Solid lines represent G_u and dotted lines represent $G_{\dot{\theta}}$

The resonance of $G_{\dot{\theta}}$, denoted as $\omega_{r,G_{d\theta}}$, where the motor velocity $\dot{\theta}$ is strongly influenced by τ_{ext}, is identical for both controllers, as shown in equations (3.53) and (3.60), and illustrated by the dotted line in Fig. 3.18. Both equations indicate a zero at the origin, resulting in a positive slope at low frequencies.

---

[9] Here, $D_\eta = 0$ is applied for ESPi, and $(K_p, K_d) = (3, 0.02)$ is used for CIC inner torque control.

At high frequencies, the effect of τ_{ext} on $\dot{\theta}$ in the CIC decreases, suggesting a theoretically high anti-resonance, whereas in the ESPi controller, this effect remains constant.

Case 2 with varying K_q

The selection of K_q has no apparent influence on the aforementioned trends in Case 1, as shown in Fig. 3.19a. The distinction lies is the magnitude of G_u^{ESPi} at resonance slightly increases, as K_q grows.

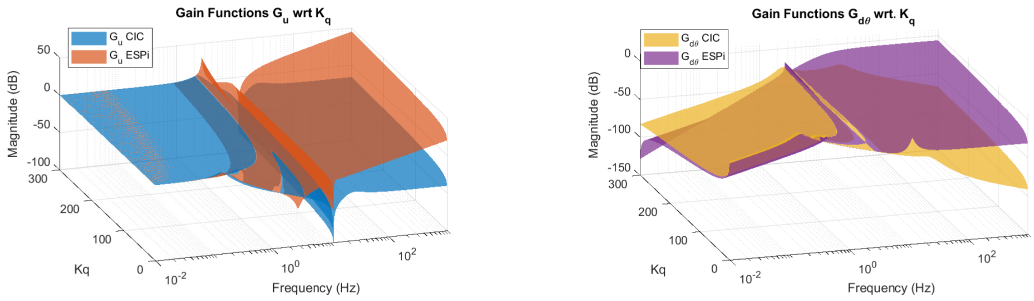

(a) G_u w.r.t. K_q

(b) $G_{\dot{\theta}}$ w.r.t. K_q

Figure 3.19: 3D comparison of gain functions wrt. K_q. (a) G_u (b) $G_{\dot{\theta}}$

The second resonance of $G_{\dot{\theta}}^{ESPi}$ becomes more pronounced with decreasing K_q, as shown in Fig. 3.19b. Conversely, the magnitude of $G_{\dot{\theta}}^{ESPi}$ diminishes as K_q increases. In contrast, the selection of K_q has little effect on $G_{\dot{\theta}}^{CIC}$ at low frequency while $G_{\dot{\theta}}^{CIC}$ decreases with decreasing K_q at high frequency.

The use cases of the controlled system under different disturbances τ_{ext} will be discussed in the section 4.3 and compared with the results from this section.

4 Augmented Analysis and User Case

4.1 Impedance Gain Selection from Passive Impedance

This section focuses on incorporating the passive impedance region into the controller design for both controllers, based on the passive impedance region analysis in section 3.1.

4.1.1 Force Cascaded Impedance Control

For the CIC parameters, the passive impedance region is first evaluated at the spring port to exclude the load dynamics. An intuitive approach can then be derived from equation (3.6). As the frequency approaches zero ($s \to 0$) and K_p is sufficiently large, K_q approximates the magnitude of $Z^{CIC}_{spring}(s)$. A transformation from decibels to N/m, simplifying later utilization, is derived from the calculation of decibels for bode plot. It is given by,

$$Z^{CIC}_{spring,N/m}|_{s \to 0} = s \cdot 10^{0.05 Z^{CIC}_{spring,dB}(s)}, \tag{4.1}$$

where $s = 2\pi f_{min}$ denotes the coordinate at the minimum allowable frequency.

This approach is named the direct retrieval approach, as it enables directly retrieve the impedance controller gain, as depicted in Fig. 4.1, where K_p is set to 7 to fulfill the K_p assumption in this method.

Beyond direct retrieval approach, the apparent impedance in any controllers reflects the chosen desired impedance as $Z_{spring} = \mathcal{H}_{spring}(Z_{des})$ and $Z_{load} = \mathcal{H}_{load}(Z_{des})$. We aim to derive the inverse relations $Z_{des} = \mathcal{H}^{-1}_{spring}(Z_{spring})$ and

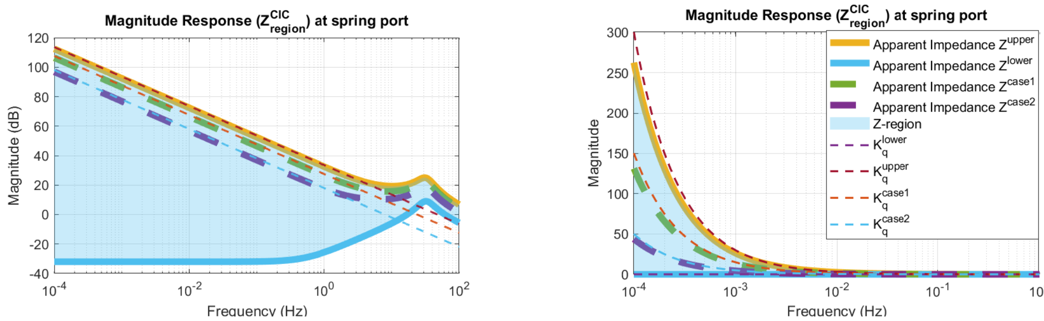

(a) Z^{CIC}_{spring} vs. K_q in dB. (b) Z^{CIC}_{spring} vs. K_q in original scale.

Figure 4.1: Z^{CIC}_{spring} vs. K_q relationships at $s \to 0$ with $K_p = 7$ and $D_q = 2\sqrt{BK_q}$ for critical damping. Thick solid lines represent passive impedance bounds, thick dotted lines validate two cases ($K_q = 50$ and $K_q = 150$), and thin dotted lines correspond to desired K_q for Z_{des}. All system parameters are from Table 3.1, except K_p.

$Z_{des} = \mathcal{H}^{-1}_{load}(Z_{load})$, mapping Z_{imp} to Z_{des} without and with load dynamics respectively. This generalized notation applies to any controller and enables determining controller parameters $[K_q, D_q]$ from the passive impedance region. Thus, it is named the indirect retrieval approach.

In CIC, the inverse relations $\mathcal{H}^{-1}_{spring}$ and $\mathcal{H}^{-1}_{load}$, derived from equations (3.1) and (3.4), are given by,

$$\begin{aligned} Z^{CIC}_{des,spring} &= \mathcal{H}^{-1}_{spring}(Z^{CIC}_{spring}) \\ &= -\frac{\left(P_m^{-1} + N^{-2}K_s + N^{-1}K_sC_f\right)s}{N^{-1}K_sC_f} Z^{CIC}_{spring} + \frac{NP_m^{-1}}{C_f}, \end{aligned} \tag{4.2}$$

$$\begin{aligned} Z^{CIC}_{des,load} &= \mathcal{H}^{-1}_{load}(Z^{CIC}_{load}) \\ &= -\frac{\left(P_m^{-1} + N^{-2}K_s + N^{-1}K_sC_f\right)}{N^{-1}K_sC_f}\left(sZ^{CIC}_{load} - P_l^{-1}\right) + \frac{NP_m^{-1}}{C_f}, \end{aligned} \tag{4.3}$$

where $Z^{CIC}_{des,spring} = Z^{CIC}_{des,load} = -K_q - D_qs$ represents the designed impedance controller. By specifying a frequency of interest, this indirect retrieval approach facilitates impedance gain selection.

To illustrate these steps, two examples of $\mathcal{H}^{-1}_{spring}$ evaluated at the spring port are highlighted in Fig. 4.2, with the frequency of 2 Hz (denoted by the blue point) being discussed first. The feasible magnitude range of Z^{CIC}_{spring} is indicated

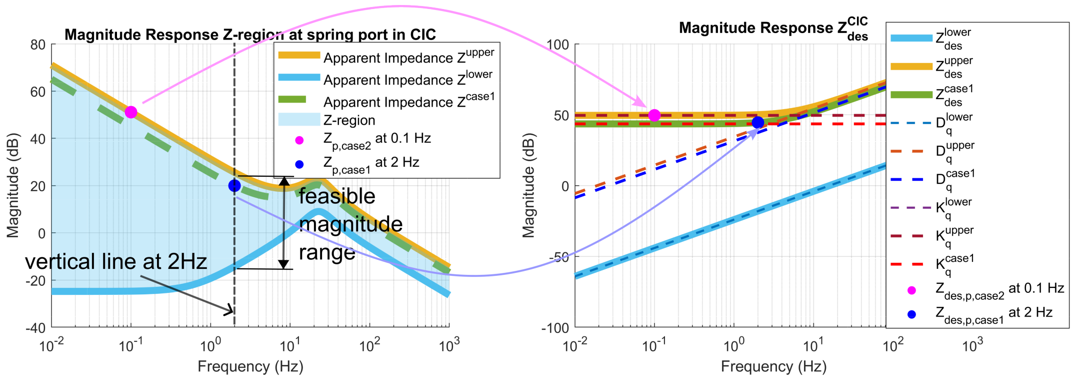

(a) (b)

Figure 4.2: Z_{spring} mapped to Z_{des} via the Z-region for CIC. The line types are consistent with those in Fig. ??.

in Fig. 4.2a, derived from the vertical line at 2 Hz within the Z-region. A desired passive apparent impedance of 19.6 dB is selected, marked as the blue point Z_{case1}.

Applying the mapping relation $\mathcal{H}_{spring}^{-1}$ in (4.2) with $s = 2\pi f$, the designed impedance gain Z_{des} is calculated and marked in Fig. 4.2b as Z_{des}^{case1}(blue point). Z_{des} comprises K_q (stiffness) and D_q (damping), represented as a horizontal line for different magnitudes and a line with a slope of 20 dB per decade, respectively.

Besides, K_q primarily influences Z_{des} at low frequencies, while D_q becomes more significant at higher frequencies. Since the chosen frequency lies in the low-frequency range, only K_q can be determined from Fig. 4.2b, where Z_{des}^{case1} corresponds to K_q^{case1}. Determining D_q requires focusing on the higher-frequency region of the passive impedance range.

Another example, with a frequency of 0.1 Hz, selects the maximum apparent impedance of 52 dB, marked in Fig. 4.2a as Z_{case2} (magenta point). The corresponding Z_{des}^{case2} represents the maximum designed K_q at 0.1 Hz.

For the direct retrieval approach, considering the load dynamics, the apparent impedance evaluated at the load port based on (3.4) converges as,

$$Z_{load}^{CIC}|_{s\to 0} = K_q \left(\frac{K_p}{K_p + 1} \right) + D_l. \tag{4.4}$$

This approach cannot directly retrieve K_q and is unsuitable when load dynamics are included. In contrast, the indirect retrieval approach based on (4.3), can determines Z_{des} from the Z-region.

4.1.2 Elastic Structure Preserving Impedance Control

For the indirect retrieval method in ESPi control, the inverse relations $\mathcal{H}^{-1}_{spring}$ and $\mathcal{H}^{-1}_{load}$, derived from equations (3.8) and (3.4), are expressed as,

$$Z^{ESPi}_{des,spring} = \mathcal{H}^{-1}_{spring}(Z^{ESPi}_{spring}) = sZ^{ESPi}_{spring} + \frac{N^2 K_s P_m^{-1}}{N^2 P_m^{-1} + K_s}, \tag{4.5}$$

$$Z^{ESPi}_{des,load} = \mathcal{H}^{-1}_{load}(Z^{ESPi}_{load}) = sZ^{ESPi}_{load} - P_l^{-1} + \frac{N^2 K_s P_m^{-1}}{N^2 P_m^{-1} + K_s}. \tag{4.6}$$

The steps of indirect retrieval method to derive the desired impedance components K_q (stiffness) and D_q (damping) in ESPi control follows the same steps as in CIC, as shown in Fig. 4.3 with two cases.

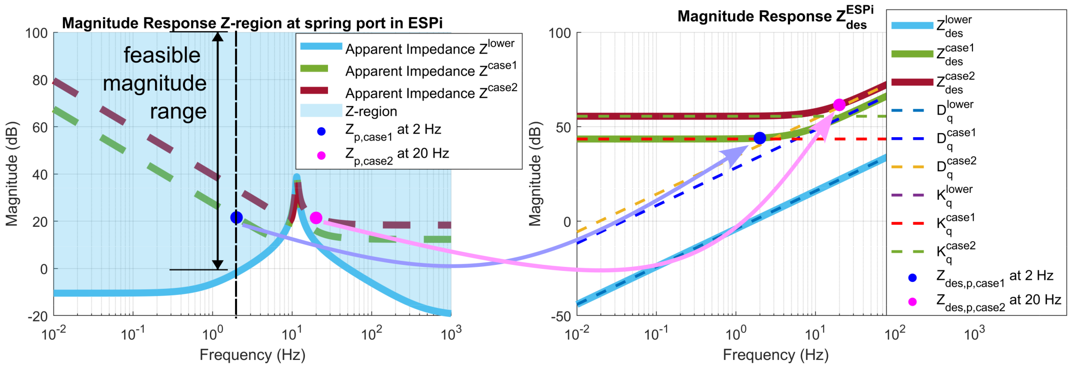

(a) (b)

Figure 4.3: Z_{spring} mapping to Z_{des} via Z-region for ESPi controller. The line types are consistent with those in Fig. 4.1.

4.2 Maximum Torque Generation influenced Passive Impedance

The impedance-controlled SEA acts as a torque source, providing equivalent impedance torque to modulate interaction forces effectively. Metrics for evaluating transmissibility are introduced in section 3.2, considering practical limitations ($\tau^{max}_{m,cont}$ and $\omega_{m,per}$). This section investigates integrating transmissibility into the passive impedance region outlined in subsection 3.1.2, enabling retrieval of the feasible torque proportional gain while ensuring maximum torque generation. The contraction of the passive impedance gain K_q as a new lower bound for the passive impedance region is discussed in subsection 4.2.1, followed by the extension of the 3D passive impedance region to incorporate the effect of the torque controller gain K_p, which reduces the feasible frequency width, as detailed in subsection 4.2.2.

For maximum torque generation under $\tau_{m,cont}^{max}$ and $\omega_{m,per}$ constraints, the ratio $\eta_{\tau,\omega}$ is critical in determining the dominance of ω_{MT} in (3.44), as discussed in subsection 3.2.3. Since the $\eta_{\tau,\omega}$ derived from Table 3.1 using equation (3.41) falls in the low region, ω_{MT_τ} and MTT_τ dominate the maximum torque frequency bandwidth in our case.

4.2.1 Contraction of Passive Impedance Gain

For the outer impedance loop, which depends solely on K_q and is independent of K_p, the contraction of passive K_q is evaluated at the load port based on the passive impedance region and MTT_τ including load dynamics. The process follows these steps:

1. Derive $\omega_{MT_\tau}^{out}$ within the K_q range $[0, 2K_s]$[1], represented as tuples $\Phi_{K_q} = (K_q^i, \omega_{MT_\tau}^{out,i})$, where $i = 1, 2, \ldots, N_1$, and N_1 is the number of sample points for the outer impedance loop. The results are shown as the black curve in Fig. 4.4a.

2. Sort Φ_{K_q} based on $\omega_{MT_\tau}^{out,i}$ to enhance computational efficiency.

3. Calculate the corresponding impedance $Z_{load}^{CIC}(s^i)$ using equations (3.1) and (3.4) for given K_q^i and s^i, denoted as $Z_{load,MT}^{CIC}(s^i) = f(K_q^i, s^i)$, where $s^i = 2\pi\omega_{MT_\tau}^{out,i}$. Calculations assume $K_p = 3$[2].

4. Interpolate the discrete values of $Z_{load,MT}^{CIC}(s^i)$ into a continuous line, illustrated as the black curve in Fig. 4.4b.

---

[1] The maximum passive apparent impedance is chosen as $2K_s$ based on experimental results in Fig. 3.4.

[2] This value is chosen as it provides the largest bandwidth for K_p, as discussed in subsection 3.2.1. Notably, while $\omega_{MT_\tau}^{outer}$ is independent of K_p, the calculation of $Z_{load}^{CIC}(s)$ depends on K_p.

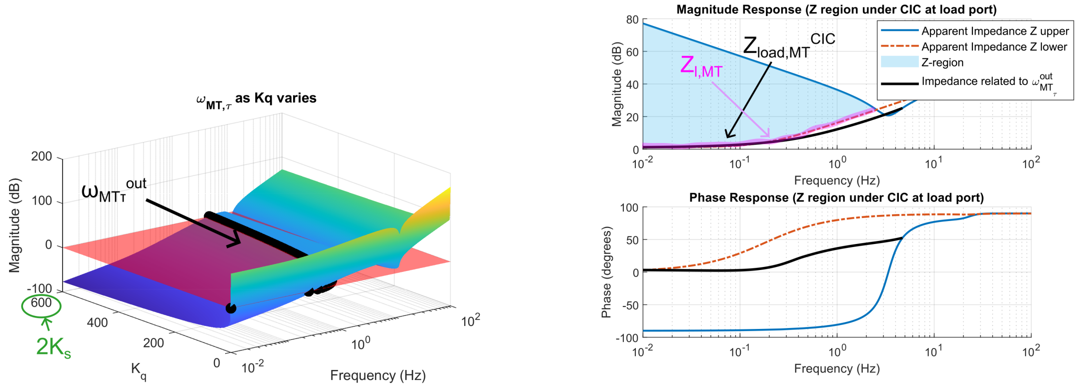

(a) ω_{MT_τ} plotted on the 3D MTT_τ w.r.t. various K_q.

(b) 2D Z-region Bode plot integrated with ω_{MT_τ}, represented by the black line. Here, K_p is set to 3.

Figure 4.4: Comparison of ω_{MT_τ} (a) on the 3D MTT_τ surface and (b) within the 2D Z-region Bode plot.

The black curve in Fig. 4.4b represents the lower bound of the impedance range required to ensure large torque generation. This is because, as K_q increases, $\omega_{MT_\tau}^{out}$ grows (Fig. 3.11) and the apparent impedance curve shifts upward (Fig. 4.2).

Each tuple Φ_{K_q} represents the minimal K_q required to ensure large torque generation at a given frequency $\omega_{MT_\tau}^{out}$. The black curve is formed by these minimal K_q values across different frequencies. Increasing K_q beyond this threshold at a given frequency guarantees large torque generation, as $\omega_{MT_\tau}^{out}$ rises with higher K_q.

The passive impedance region slightly decreases due to the black curve derived from Φ_{K_q}, as shown in Fig. 4.4b. The overall lower boundary for passive impedance region, ensuring large torque generation, is defined as,

$$Z_{l,MT}(s) = \max\left(\left|Z_{load}^{lower}(s)\right|, \left|Z_{load,MT}(s, K_q)\right|\right), \tag{4.7}$$

that is highlighted as the magenta thick curve in the figure.

4.2.2 Retrieval Feasible Torque Proportional Gain

For the inner torque loop, the feasible frequency range is determined by the corresponding K_p. Therefore, it is essential to identify the two bounds, $\omega_{MT_\tau}^{inn}$ and

$\omega_{MT_\tau}^{inn,lower}$, as discussed in subsection 3.2.1. The process to achieve this follows these steps[3]:

1. Derive $\omega_{MT_\tau}^{inn}$ and $\omega_{MT_\tau}^{inn,lower}$ within the K_p interest range $[0, 50]$, represented as tuples $\Phi_{K_p} = (K_p^i, \omega_{MT_\tau}^{inn,i})$ for $i = 1, 2, \ldots, N_2$, where N_2 is the number of sample points, and $\Phi_{K_p,lower} = (K_p^i, \omega_{MT_\tau}^{inn,lower,i})$ for $i = 1, 2, \ldots, N_3$, where N_3 denotes the number of sample points. $\omega_{MT_\tau}^{inn}$ is shown as the black curve, and $\omega_{MT_\tau}^{inn,lower}$ is illustrated as the blue curve in Fig. 4.5a[4].
2. Calculate $Z_{load,MT}^{CIC}(s^i) = f(K_q^i, s^i, K_p^j)$, where each K_p^j defines its own plane with $s = 2\pi\omega_{MT_\tau}^i$ for various K_q. This results in a 2D passive impedance region for each K_p, as shown in Fig. 4.4b.
3. Combine the multiple 2D planes of $Z_{load,MT}^{CIC}(s^i)$ derived in the previous step across K_p to form a 3D volume, as illustrated in Fig. 4.5b. The red surface represents the lower bound of the impedance range corresponding to K_q.
4. Interpolating $\omega_{MT_\tau}^{inn}$ and $\omega_{MT_\tau}^{inn,lower}$ respectively forms two constraint plane, depicted as the green surfaces in Fig. 4.5b.

The actuator limitations constrain K_q by the lower bound of the passive impedance region, depicted as the red surface in Fig. 4.5b, and by the upper and lower bounds of the feasible frequency width ω_{LFB}, introduced in subsection 3.2.1 and illustrated as the green surface. To maximize ω_{LFB} within the passive impedance region, K_p should lie between 0.1 and 7.2, aligning with the observation in Fig. 3.11. Conversely, to maximize the passive impedance region, a larger K_p is preferable, as observed in Fig. 3.7b, indicating a tradeoff between ω_{LFB} and the Z-region.

4.3 Energy efficiency Results

To identify the most energy-efficient controllers for SEA under disturbance, the objective is to determine the control strategy that minimizes maximum control effort,

---

[3] The steps outlined for the outer impedance loop K_q in the previous subsection are also applicable here

[4] Notably, the result in Fig. 4.5a aligns with the tendency of MTT_τ with respect to K_p, encompassing both the normal $\omega_{MT_\tau}^{inner}$ and the lower bound $\omega_{MT_\tau}^{inner,lower}$, as depicted in Fig. 3.11.

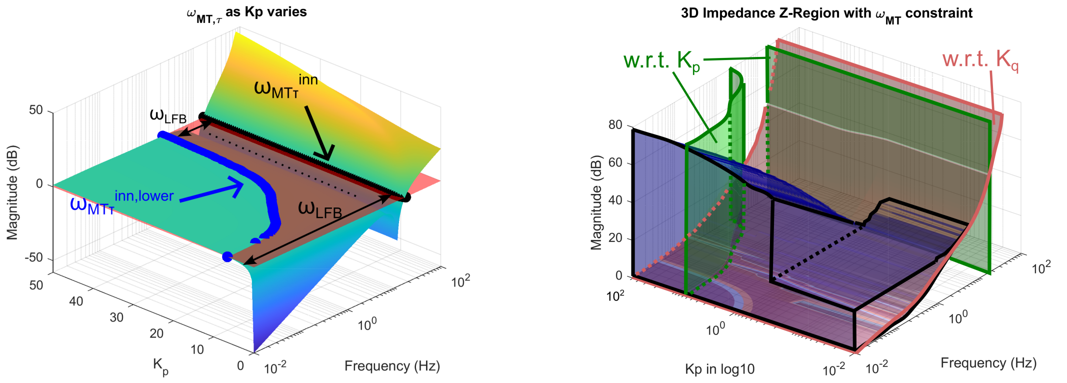

(a) ω_{MT_τ} and $\omega_{MT_\tau}^{inner,lower}$ plotted on the 3D MTT_τ with respect to various K_p. Here, K_q does not affect the value of ω_{MT_τ} and $\omega_{MT_\tau}^{inner,lower}$.

(b) 3D Z-region Bode plot integrated with ω_{MT_τ} with respect to K_q (red plane) and K_p (green planes). Here, K_p is expressed on a logarithmic scale.

Figure 4.5: (a) ω_{MT_τ} and $\omega_{MT_\tau}^{inner,lower}$ plotted on the 3D MTT_τ. (b) 3D Z-region Bode plot integrated with ω_{MT_τ}.

denoted as $\tau_{m,max}$ and $\bar{P}$ under various disturbance conditions. Two regulation control cases are discussed below.

4.3.1 Periodic Disturbance on Regulation Control

The first case without friction is analyzed under the condition that τ_{ext} is a periodic sinusoidal signal with a specific frequency f_{Hz}. The analysis focuses on the first 10 seconds, with $\tau_{ext} = 3\sin(2\pi f_{Hz} t)$, where the amplitude is set to 3 Nm.

The maximum control input with respect to varying desired K_q and the specified f_{Hz}, as shown in Fig. 4.6, aligns with the inference from the transfer functions G_u^{CIC} and G_u^{ESPi} in subsection 3.3.3. The resonance of both controllers results in a peak control input. Furthermore, the 2D plot of K_q versus u_{max} demonstrates that as K_q increases, u_{max} also grows.

The absolute peak power with respect to varying desired K_q and the specified f_{Hz}, as illustrated in Fig. 4.7, aligns with the behavior of the gain functions $G_{\dot{\theta}}^{CIC}$ and $G_{\dot{\theta}}^{ESPi}$ in subsection 3.3.3. The power is calculated by integrating G_u multiplied by $G_{\dot{\theta}}$, where the dominant influence on the overall trend is $G_{\dot{\theta}}$ based on the observation. The two peaks in Fig. 4.7 correspond to the resonance frequencies

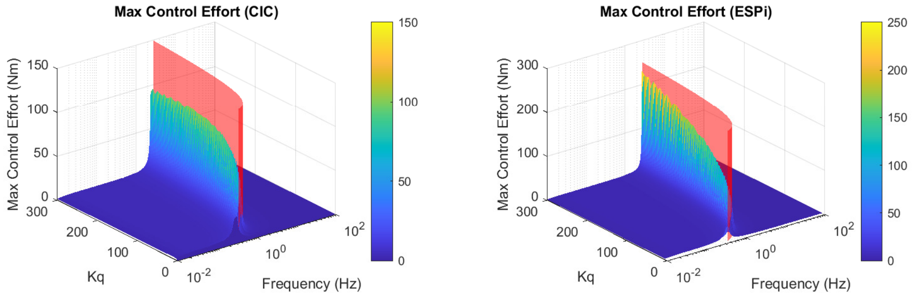

Figure 4.6: Maximum control input under τ_{ext}, modeled as a periodic sinusoidal signal over 10 seconds. The red surface indicates the first resonance of each controller separately. The results are based on equations (3.51) and (3.58).

of the respective controllers, which matches our inference in subsection 3.3.3.

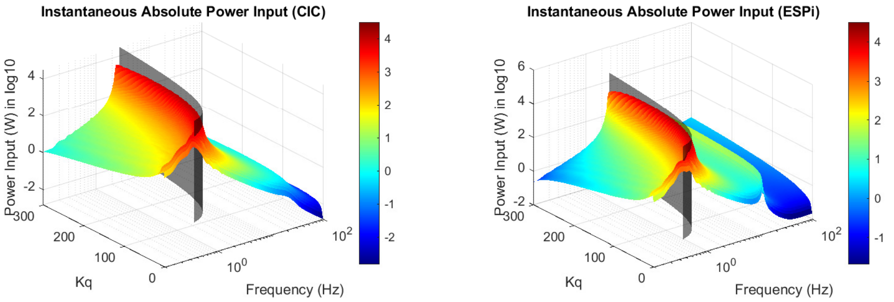

Figure 4.7: Peak power input under the same conditions as Fig. 4.6. The results are based on equations (3.53) and (3.60).

4.3.2 Sudden Contact Force on Regulation Control

The second case with friction assumes τ_{ext} as a contact force modeled by a half sine wave [81, 84]. The goal is to maintain the output position at the equilibrium point and analyze the energy and control input required to preserve the desired impedance behavior under a sudden contact force. In the following analysis, the maximal sudden contact input is set to 100 Nm, the desired K_q is 50, and the remaining parameters are the same as those in Table 3.1.

The CIC-controlled system exhibits larger deflection but lower instantaneous power, whereas the ESPi-controlled system converges faster with higher instanta-

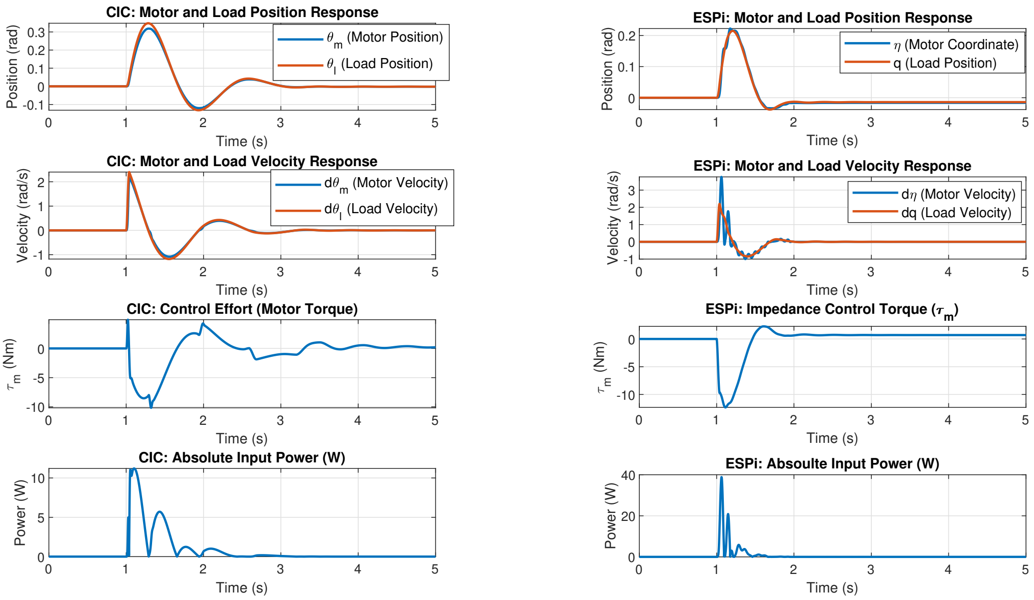

(a) CIC

(b) ESPi Control

Figure 4.8: Response of the controlled SEA system to a sudden contact force, which occurs at $t = 1$ s. The desired K_q is set to 50.

neous power and velocity, as shown in Fig. 4.8. Over 5 seconds, both controlled systems have total energy inputs on the order of 10^3, with ESPi at 3.23×10^3 and CIC at 3.77×10^3, indicating that ESPi is slightly more energy-efficient under this configuration.

To enhance versatility, the influence of the desired impedance gain on the absolute input power and overall control input is analyzed in Fig. 4.9. As K_q increases, the maximal instantaneous power grows for both controllers, except for a bulge at very low K_q in CIC. The overall instantaneous power for ESPi is higher than for CIC, likely due to the faster convergence speed of ESPi. However, the total energy input for ESPi is lower than for CIC, indicating greater energy efficiency in this case, as shown in Fig. 4.10.

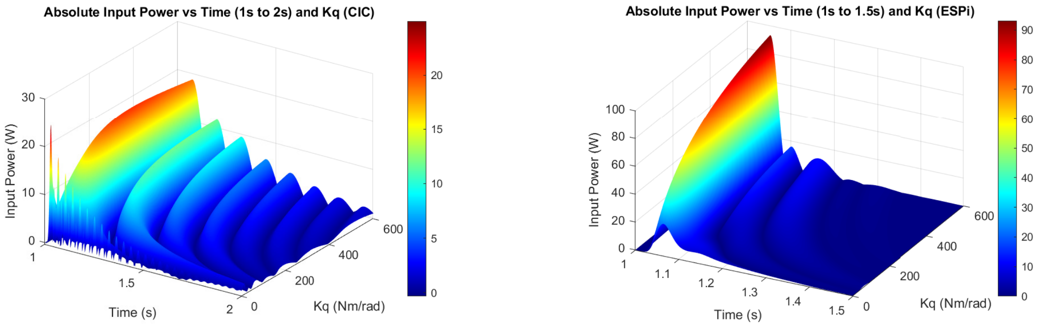

(a) CIC for interest time snippet $t = 1s\ 2s$

(b) ESPi Control for interest time snippet $t = 1s\ 1.5s$

Figure 4.9: Response of the controlled SEA system to a sudden contact force occurring at $t = 1$ s with respect to varying K_q.

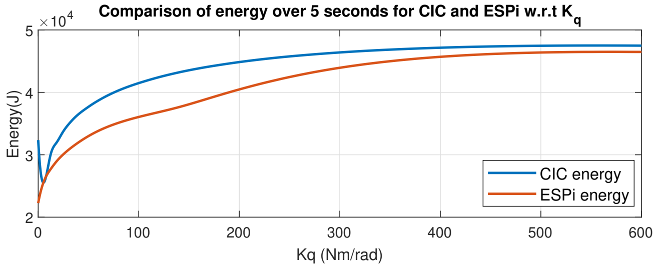

Figure 4.10: Comparison of energy consumption w.r.t. K_q for CIC and ESPi

4.3.3 Conclusion

In the first case, the maximum control input $\tau_{m,\max}$ and the peak of instantaneous absolute power for CIC are smaller than those for ESPi control, indicating lower peak input power and reduced stress on the actuator. In the second case, the peak absolute power for ESPi control exceeds that of the CIC, which may result in higher transient loads on the actuator. However, the overall energy input for ESPi control is smaller than that for CIC, demonstrating greater energy efficiency over time. Besides, the consideration of friction does not affect the overall tendency of the control input and power. Overall, ESPi control is more energy-efficient, while CIC is preferable for minimizing peak values.

5 Testbed and Identification

5.1 Testbed Configuration

The testbed configuration consists of two main components: hardware and software (including communication), introduced in subsections 5.1.1 and 5.1.2, respectively.

5.1.1 Hardware Setup

The hardware setup underwent three iterations over eight months. The first version, primarily constructed from 3D-printed materials, exhibited slightly elastic characteristics, as shown in Fig. 5.1. However, the output was directly connected to the ground, lacking a buffer, which made the SEA system's spring prone to breakage.

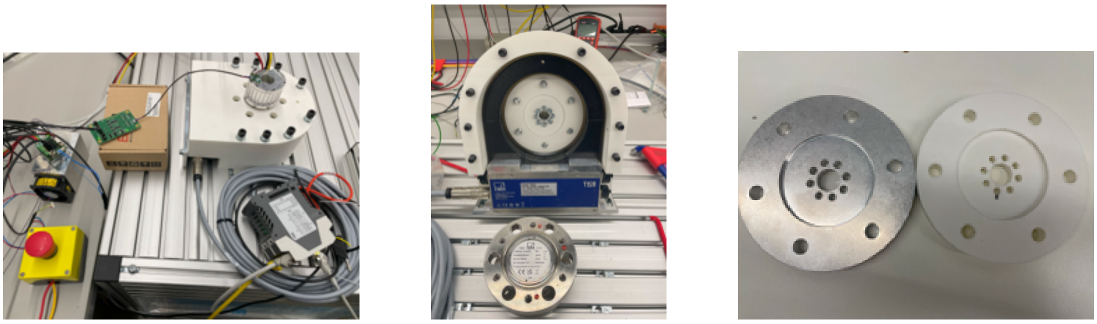

(a) Overall configuration

(b) Without shell

(c) Connection (left: aluminum, right: 3D print)

Figure 5.1: Initial Testbed: (a) Overall configuration; (b) Without shell; (c) Connection materials comparison.

The second version replaced the 3D-printed materials with aluminum and added a coupling for actuator connections to reduce vibrations, as shown in Fig. 5.2. However, the output configuration remained the same as the initial setup, leaving the risks unchanged. In both the first and second setups, the actuator was directly controlled via an Elmo Gold Twitter servo drive, and a torque sensor (H40B) was positioned at the output port, utilizing electromagnetic induction and connected to a torque transducer for measurement processing.

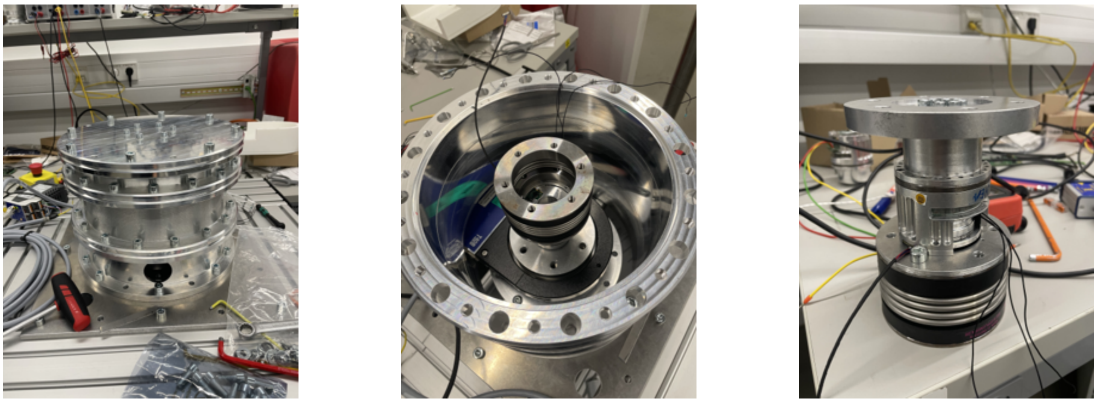

(a) Overall configuration (b) Without shell (c) Actuator

Figure 5.2: Second Version Testbed: (a) Overall configuration; (b) Without shell; (c) Actuator with connection.

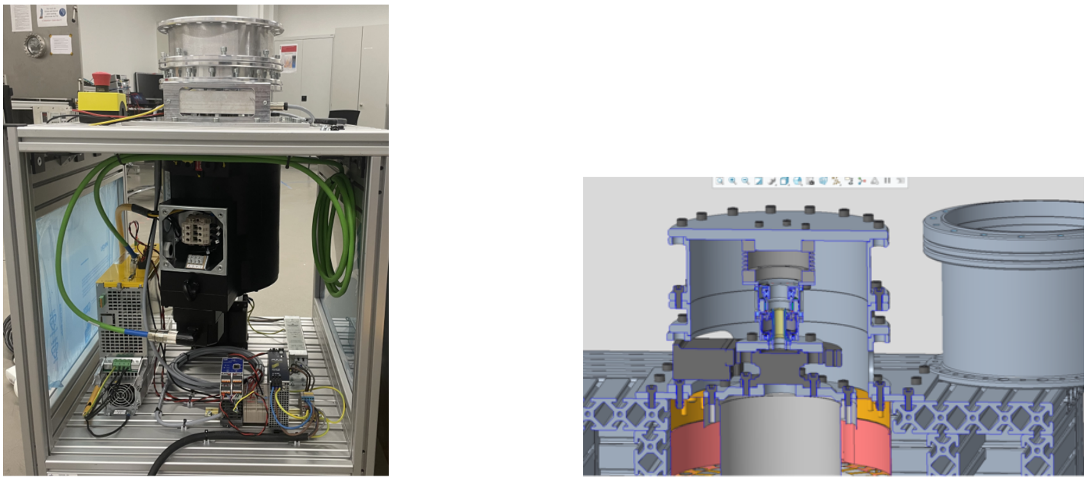

(a) Overall Configuration (b) CAD Representation

Figure 5.3: Final Testbed: (a) Overall setup. (b) CAD representation.

The final version addresses the drawbacks of previous setups by connecting the output to a larger actuator, capable of generating high direct output torque for simulating various environmental scenarios, as shown in Fig. 5.3. The output actuator is directly controlled via the Baumueller drive. This configuration is designed to create a high-torque, low-velocity testing environment for future evaluating the performance of the tested actuators.

5.1.2 Software Setup

In order to utilize the existing links-and-nodes interface and robotkernel in our institute, which is similar to ROS, the software for the testbed is designed to establish communication between the testbed and the real-time PC, trigger the process to bring the testbed into operation, log all measured and commanded data from encoders and sensors, and control actuators in different modes. An overview of the software and hardware configuration is shown in Fig. 5.4.

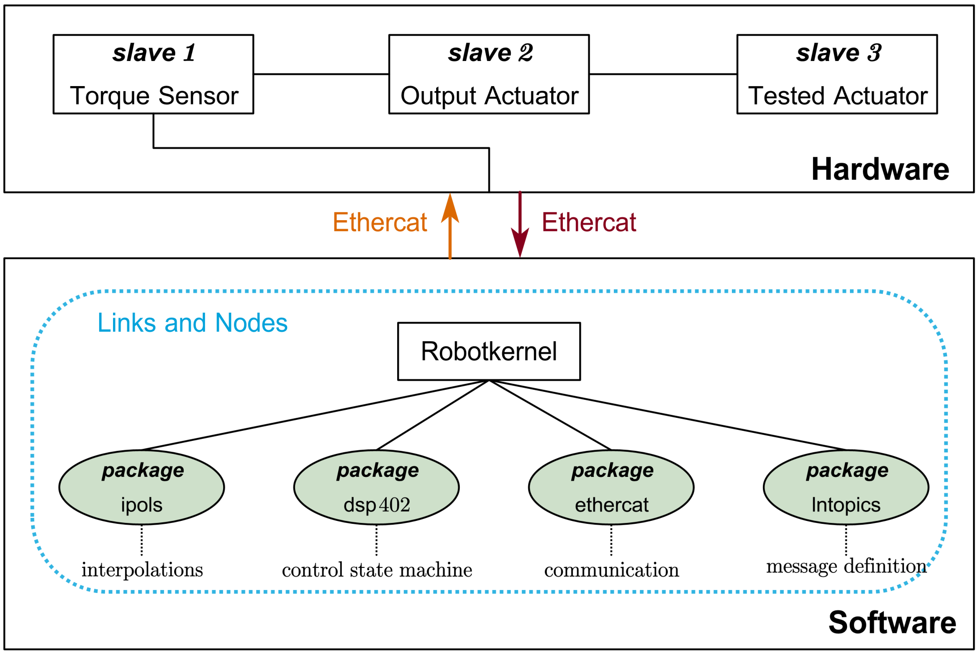
slave 1
Torque Sensor
slave 2
Output Actuator
slave 3
Tested Actuator
Hardware
Ethercat
Ethercat
Links and Nodes
Robotkernel
package
ipols
package
dsp402
package
ethercat
package
lntopics
interpolations
control state machine
communication
message definition
Software

Figure 5.4: Relationship between hardware and software in the testbed configuration

The software of the testbed includes mainly four packages: `ipols` for input value interpolation (e.g., command), `dsp402` for the standard 402 control state machine to trigger controllers on the Elmo and Baumueller drivers, `ethercat` for software-to-hardware communication, and `lntoptics` for defining and delivering messages between slaves and masters.

There are three EtherCAT slaves: the torque sensor, the output actuator (Baumueller), and the tested actuator, sequentially. Once the process on the links-and-nodes interface at the user PC is triggered, the EtherCAT communication undergoes four phases: *init*, *pre-op*, *safe-op*, and *op*. During operation, the system exchanges messages, including `torque_measured`, `elmo_cmd`, `elmo_measured`, `baumueller_cmd`, and `baumueller_measured`, at the real-time PC (Host).

The delivery and sampling rate is set to 1 kHz, which is sufficient for the identification experiments. The DSP402 supports three control modes: position, velocity, and current mode. For the tested actuator, three modes are implemented, allowing commands to be easily issued through various function calls.

5.2 Identification Results

5.2.1 Stiffness Approximation

Elastic stiffness K_s can be identified by rotating the actuator back and forth, triggering the resulting hysteresis behavior [15]. The experiment is conducted under two cases with continuous sinusoidal current input: varying amplitudes at a fixed frequency (approximately 0.1 Hz) and varying frequencies at a fixed amplitude (approximately 5 Amps). Notably, the output is directly connected to the ground, indicating that q in (2.1) as 0, and the spring deformation directly corresponds to the motor position θ.

Under the same amplitude, the derived stiffness is approximately 287 Nm/rad, while the measured K_s slightly increases with smaller amplitude inputs, as shown in Fig. 5.5a, possibly due to nonlinear stiffness behavior or friction effects that become more dominant at lower amplitudes. On average, the stiffness is 297 Nm/rad with no apparent hysteresis behavior, closely matching the target stiffness of 313 Nm/rad composed of glass fiber, as shown in Fig. 5.5b.

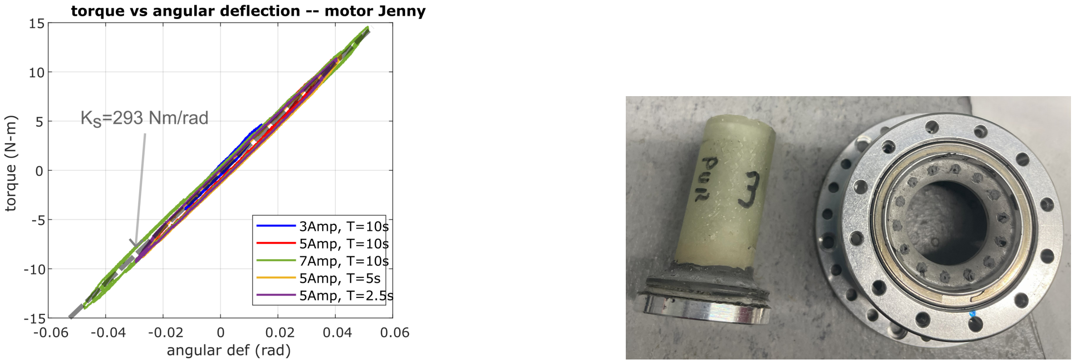

(a) Identified stiffness: output torque vs displacement

(b) actual stiffness

Figure 5.5: (a)Identified stiffness: output torque vs displacement (b)actual stiffness in actuator

5.2.2 Residual Friction

Based on friction foundation in subsection 2.1.2, the ideal friction models utilized in this subsection are depicted in Fig. 2.1. In theory, identifying static friction models requires experiments conducted under constant velocity modes to eliminate acceleration effects [16, 17, 15], while dynamic friction models are identified using chirp input signals to excite the system [14].

Our experiment is conducted by given the chirp input current from 0.01 Hz to 20 Hz over 120 seconds with amplitude as 3 Amp[1]. Remarkably, the setup is same as in subsection 5.2.1, output connect to ground.

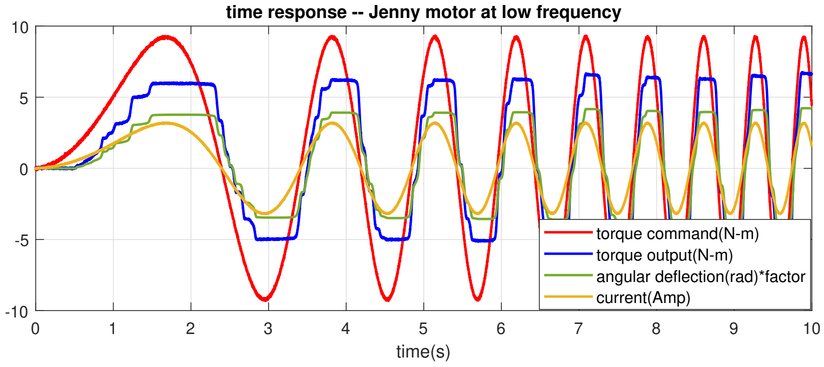

(a) lower frequency range (snippet for 15s)

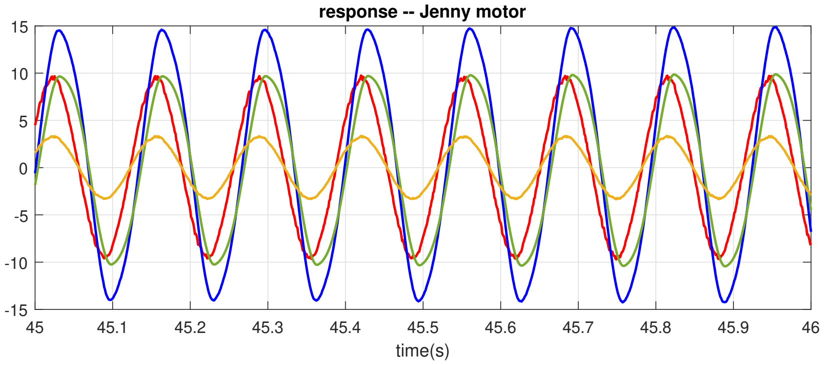

(b) higher frequency range (snippet for 1s)

Figure 5.6: time-domain response (a) in the low frequency range (b) in the high frequency range. Here, the sample rate is 1kHz.

---

[1] The torque constant, denoted as k_T, is 2.9, found in the datasheet. To obtain the motor input torque τ_m equals the product of input current and k_T.

To better understand the system's overall dynamics, it is necessary to investigate the time-domain response. At low frequencies, the stick-slip motion is pronounced, causing the system to remain in the stick phase, resulting in an unsmooth curve, as shown in Fig. 5.6a. Additionally, the system response is dominated by the friction force. In contrast, at high frequencies, the output curve becomes smoother due to the absence of stick-slip motion, as depicted in Fig. 5.6b.

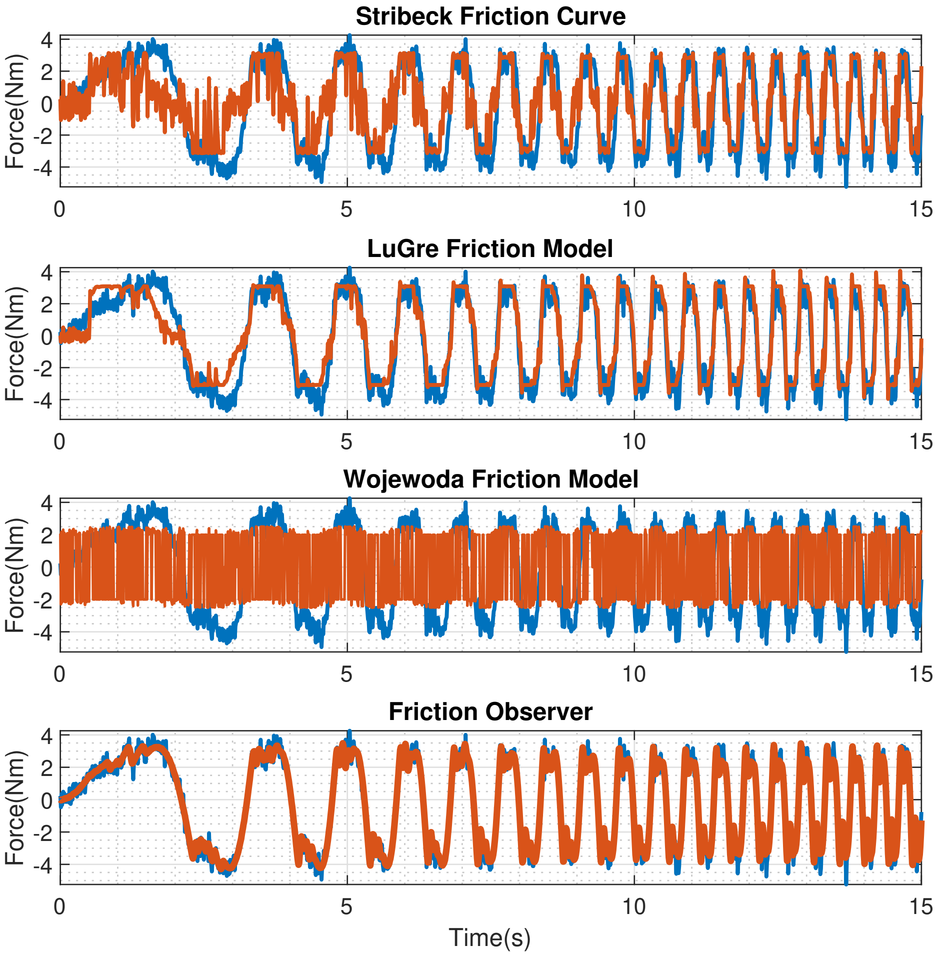

Figure 5.7: Fitted friction model: τ_{fric} versus time. Sample rate 100 Hz

Due to the Stribeck effect in residual friction, the fitted models include the Stribeck curve, LuGre model, and Wojewoda model, using MATLAB's *fmincon* function with a positivity constraint. To avoid complexities of high-frequency dynamics, experimental data were fitted at low frequencies presented in Fig. 5.6a, assuming the friction force equals $(\tau_m - \tau_s)$ minus the inertia force[2]. The identified results are presented in Appendix B.

At low frequencies, stick-slip motion causes all three models (Stribeck, LuGre, Wojewoda) to poorly predict friction forces, though the LuGre model performs better, as shown in Fig. 5.7. At higher frequencies, the LuGre and Stribeck models approximate the friction magnitude, but the Stribeck model exhibits bulges near zero force during velocity changes. The Wojewoda model, despite theoretical alignment with experimental data, fails in practice, showing dramatic force fluctuations in Fig. 5.7.

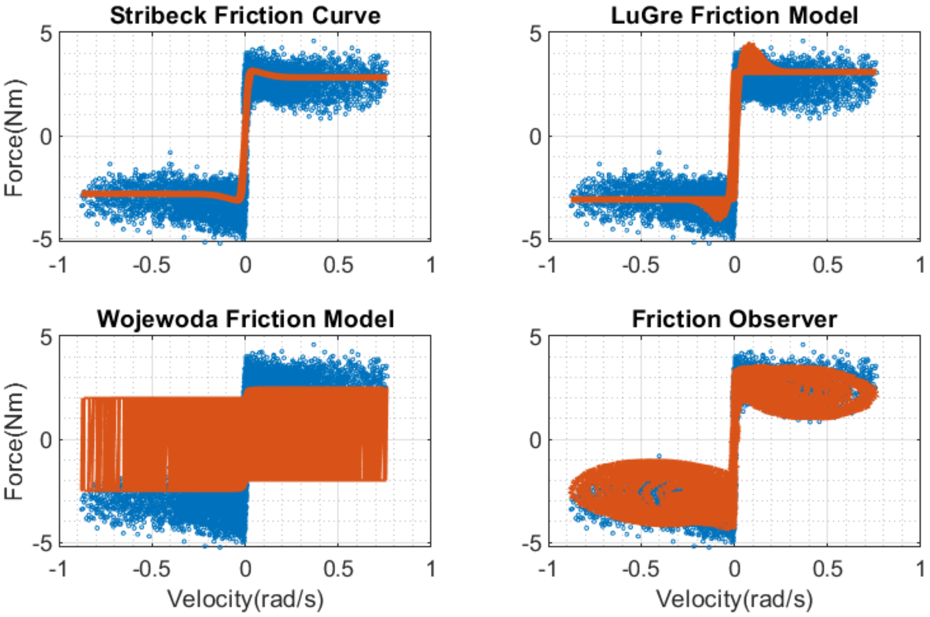

Figure 5.8: Fitted friction model: τ_{fric} versus velocity.

Similar fluctuations are observed in the Wojewoda model's velocity response, indicating that the relationship between acceleration and velocity is insufficient to reliably determine the friction phase in (4), as depicted in Fig. 5.8. In conclusion, the LuGre model, with its internal state representation, provides the best identification results for velocity and time response.

---

[2] The inertia force was computed by numerically differentiating acceleration from measured θ, neglecting the damping term.

Current research offers control strategies to mitigate inaccuracies in model-based compensation, often referred to as the motor disturbance observer (mDoB) or friction observer (FoB) [85]. The FoB accurately captures friction dynamics, as shown in Fig. 5.7 and Fig. 5.8, effectively addressing the complexity of friction behavior. However, the FoB has drawbacks: it requires an additional distal sensor compared to friction modeling alone, and at higher velocities, the time delay introduced by the FoB can cause further challenges.

6 Conclusion and Outlook

6.1 Conclusion

In this thesis, the testbed hardware and software are setup, actuator parameters are identified in the testbed and the metrics and measures used to evaluate the CIC and ESPi controlled systems are introduced, focusing on three perspectives: apparent passive impedance, torque/force transmissibility, and energy efficiency under disturbance. These evaluations provide a basis for selecting the optimal controller for different use cases.

To ensure passivity and system stability, the apparent impedance evaluated at the spring port in CIC is limited by the condition $K_q \leq K_s$, representing the upper-bound maximum passive desired impedance gain. In contrast, ESPi control imposes no restrictions on the selection of controller parameters, enabling ESPi to theoretically achieve a larger passive impedance region (Z-region). Moreover, the apparent impedance evaluated at the load port provides a larger Z-region for both controllers, which can be explained using the circuit representation of the SEA system. To extend the passive impedance region for CIC, a larger K_p is preferable.

To guarantee maximum torque generation under the actuator limitations $\tau_{m,cont}^{max}$ and $\omega_{m,per}$, the optimal selection of CIC controller parameters follows these rules: greater K_q and smaller K_p result in a larger feasible frequency width ω_{LFB}, as determined by MTT_τ and $\omega_{MT,\tau}$. However, based on MTT_ω and $\omega_{MT,\omega}$, the ratio $\zeta_{\tau,\omega}$, which is related to the chosen actuator datasheet, decreases. To enlarge the feasible frequency width, the selection of K_q and K_p remains consistent with the criteria for MTT_τ and $\omega_{MT,\tau}$. In practice, this means that increasing K_q while keeping K_p small allows the actuator to handle a wider frequency range of disturbances while maintaining effective torque transmission.

For energy efficiency under disturbance, the controlled system requires the most energy and exhibits the maximum peak control input to achieve the desired impedance and maintain regulation performance when the disturbance occurs at the resonance frequency for both controllers. Furthermore, as K_q increases, the system's energy consumption slightly increases. For sudden contact forces, ESPi requires less overall input energy but results in higher peak values compared to CIC, regardless of the desired K_q.

A key contribution of this thesis is the practical application of the introduced metrics. By utilizing the passive impedance region, controller parameters can be systematically designed based on apparent passive impedance using two newly proposed methods: direct retrieval and indirect retrieval. Furthermore, integrating the passive impedance region with the concept of maximum torque generation provides deeper insights, enabling the retrieval of apparent impedance under more conservative constraints. These methodologies provide a structured approach to controller parameter selection, enhancing the practical evaluation of impedance-controlled actuators across robotic systems.

It is concluded that this thesis provides the foundation for establishing unified metrics in the future and combining them with practical applications for future controller parameter selection across different actuators. This makes the evaluation of controlled actuators more structured and straightforward.

6.2 Outlook

Future research should focus on experimental validation of the proposed theoretical metrics, particularly addressing the three evaluation aspects: apparent impedance, torque transmissibility, and energy efficiency. For the ESPi controller, while the passive apparent impedance is theoretically unbounded, experimental observations suggest the existence of an upper limit, which requires further study. Additionally, the energy efficiency analysis should incorporate nonlinear effects, such as backlash, which were not considered in the current discussion. Identification experiments for inertia, which were not completed due to time constraints, also remain an important area for investigation.

Another avenue for future work involves implementing a friction observer to enable friction compensation in impedance controllers. Lastly, a long term objective is to establish unified metrics for controller evaluation, facilitating the categorization of actuators and simplifying the selection of appropriate actuator modules for various applications.

Appendix

A Friction Models

A.1 Coulumb Friction model

The Columb friction model is given by,

$$F_{\text{fric}} = \begin{cases} F_c \operatorname{sgn}(v), & \text{if } |v| \neq 0, \\ \min\left(|F_e|, F_c\right), & \text{if } |v| = 0 \end{cases} \tag{1}$$

where F_e, F_c, and v represent the external force, the magnitude of Coulomb friction, and the contact velocity, respectively.

A.2 Stribeck Curves in Gaussian Expression

The Stribeck curve is given by,

$$F_{\text{fric}} = \begin{cases} \operatorname{sgn}(v)\left(F_c + (F_s - F_c)e^{-\left(\frac{v}{v_s}\right)^2}\right), & \text{if } |v| \neq 0, \\ \min\left(|F_e|, F_c\right), & \text{if } |v| = 0 \end{cases} \tag{2}$$

where F_s and v_s denote the stiction friction and Stribeck velocity, respectively.

A.3 Lugre Model

The LuGre model is given by,

$$\begin{aligned} F_{\text{fric}} &= \alpha_0 z + \alpha_1 \frac{dz}{dt} + \alpha_2 v, \\ \frac{dz}{dt} &= v - \frac{|v|}{g(v)} z, \end{aligned} \tag{3}$$

where α_0 and α_1 are the stiffness and microdamping coefficients, respectively, and $\alpha_2 v$ represents viscous friction. $g(v)$ is the Stribeck function from above, incorporating the Stribeck effect.

A.4 Wojewoda Friction Model

The Wojewoda friction model is given by,

$$F_{fric} = \begin{cases} f_{st}\,\mathrm{sgn}(v) & \text{for } f_{st} < f_{d+} \text{ and } \mathrm{sgn}(v\dot{v}) > 0, \\ f_{d+}\,\mathrm{sgn}(v) & \text{for } f_{st} > f_{d+} \text{ and } \mathrm{sgn}(v\dot{v}) > 0, \\ f_{d-}\,\mathrm{sgn}(v) & \text{for } \mathrm{sgn}(v\dot{v}) < 0 \end{cases} \tag{4}$$

shows composition of multiple dynamics friction variants under various dynamic conditions, where f_{st}, f_{d+}, and f_{d-} represent the dynamical friction functions during compliant contact, acceleration, and deceleration phases, respectively.

B Identified friction parameters

These tables present the results for the identified friction models: the Stribeck curve, LuGre model, and Wojewoda friction model, sequentially.

Table 1: Fitted Parameters for the LuGre Model as defined in equation (3).

Parameter	α_0	α_1	α_2
Value	1.0000×10^4	86.6759	1.6043×10^{-7}
Parameter	F_c	F_s	v_s
Value	3.0876×10^{-4}	0.0408	2.2204×10^{-14}

Table 2: Fitted Parameters for the Stribeck Model as defined in equation (2), incorporating $\tanh(\alpha v)$ for smoother behavior around zero velocity.

Parameter	F_c	F_s	v_s	α
Value	2.8239	3.1870	0.1235	80.0218

Table 3: Fitted Parameters for the Wojewoda Model as defined in equation (4).

Parameter	F_c	F_s	k_s	v_a	γ	δ_{F_s}
Value	2.5000	3.0000	5.5000×10^4	0.0200	0.0020	1.0000

C Lists of Symbols

B: motor inertia

C_f: force/controller PD gain and CIC torque controller gain

D_l: link damping

D_m: motor damping

D_q: desired impedance derivative gain

f_{des}: desired force reference

f_{out}: system output force

G_u^{CIC}: transfer function relating control input to external torque under the CIC-controller system

G_u^{ESPi}: transfer function relating control input to external torque under the ESPi-controller system

G_θ^{CIC}: transfer function relating the motor position θ to external torque under the CIC-controller system

G_θ^{ESPi}: transfer function relating the motor position θ to external torque under the ESPi-controller system

$G_{\dot{\theta}}^{CIC}$: transfer function relating motor velocity $\dot{\theta}$ to external torque under the CIC-controller system

$G_{\dot{\theta}}^{ESPi}$: transfer function relating motor velocity $\dot{\theta}$ to external torque under the ESPi-controller system

K_d: the derivative gain of CIC torque controller

$K^{imp}_{max,q}$: the maximum K_q corresponding to Z_u which preserves passivity in the apparent impedance

$K^{imp}_{min,q}$: the minimum K_q corresponding to Z_l which preserves passivity in the apparent impedance

K_p: the proportional gain of CIC torque controller

K_q: desired impedance proportional gain

K_s: linear stiffness

M: link inertia

MTT_τ: maximum torque transmissibility

MTT^{inn}_τ: the MTT_τ derived from the inner control path for CIC

MTT^{out}_τ: the MTT_τ derived from the outer control path for CIC

MTT_ω: maximum velocity transmissibility

MTT^{inn}_ω: the MTT_ω derived from the inner control path for CIC

MTT^{out}_ω: the MTT_ω derived from the outer control path for CIC

N: gear ratio

P_d: the transfer function relating disturbance τ_{ext} to the link side position q

P_l: link-side dynamics

P_m: motor-side dynamics

P_q: the transfer function relating the control input to the link side position q

P_τ: the transfer function relating the control input to the output torque τ_s

P_{ω_m}: the transfer function relating the control input to the motor velocity ω_m

q: link displacement

q_d: link side position reference

R: robustness of the system

S): sensitivity of the system

S^{CIC}: sensitivity of the CICled system

S^{ESPi}: sensitivity of the ESPi controlled system

sq: output velocity (link velocity)

$T(s)$: torque/force transmissibility

u: control input in section 3.2

u_{inn}: the control input derived from the inner loop control laws for CIC

u_{out}: the control output derived from the outer loop control laws for CIC

$W(\omega)$: weighting function for Z_{region}

Y_q: coefficient of the τ_m for ESPi related to q

Y_τ: coefficient of the τ_m for ESPi related to τ_{ext}

Y_r: coefficient of the τ_m for ESPi related to q_d

Z_{des}: desired impedance

$Z^{CIC}_{des,load}$: desired impedance derived from the apparent impedance Z_{load} evaluated at the CIC-controlled system

$Z^{ESPi}_{des,load}$: desired impedance derived from the apparent impedance Z_{load} for ESPi control

$Z^{CIC}_{des,spring}$: desired impedance derived from the apparent impedance Z_{spring} evaluated at the CIC-controlled system

$Z^{ESPi}_{des,spring}$: desired impedance derived from the apparent impedance Z_{spring} evaluated at the ESPi-controlled system

Z_{imp} or Z: impedance

Z_l: the lower boundary of achievable passive impedance in the definition of Z_{region}

$Z_{l,MT}$: the overall lower boundary for passive impedance region, ensuring large torque generation

Z_{load}: the apparent impedance evaluated at the load port

Z_{load}^{CIC}: the apparent impedance evaluated at the load port for CIC

Z_{load}^{ESPi}: the apparent impedance evaluated at the load port for ESPi control

$Z_{load,MT}^{CIC}$: impedance derived by using Z_{load}^{CIC} with given $[K_q^i, \omega_{MT_\tau}^{out,i}]$

Z_{region}: Z-region or passive impedance region

Z_{spring}: the apparent impedance evaluated at the spring port

Z_{spring}^{CIC}: the apparent impedance evaluated at the spring port for CIC

Z_{spring}^{ESPi}: the apparent impedance evaluated at the spring port for ESPi control

Z_u: the upper boundary of achievable passive impedance in the definition of Z_{region}

$\bar{P}$: absolute power

$\bar{P}^{CIC}$: absolute power for CIC

$\bar{P}^{ESPi}$: absolute power for ESPi control

$\bar{u}$: the new control input from the motor side for ESPi control

β: desired impedance torque/force

η: the new motor coordinate for ESPi control

ζ_q: a variable as the ratio between K_q and K_s

$\zeta_{\tau,\omega}$: the ratio of $\tau_{mc,max}$ to $\omega_{m,per}$

ω_l: the lower frequency limits over the frequency range in the definition of Z_{region}

ω_u: the upper frequency limits over the frequency range in the definition of Z_{region}

ω_m: motor velocity in section 3.2

$\omega_{m,per}$: maximum permissible motor velocity

ω_n: natural frequency of uncontrolled SEA

$\omega_{r,d\theta}$: resonance of $G_{\dot{\theta}}$

ω_{r,G_u}: resonance of G_u

ω_{anti,G_u}: anti-resonance of G_u

ω_{MT}: maximum torque frequency bandwidth

ω_{MT}^{lower}: lower frequency boundary of maximum torque frequency bandwidth

ω_{MT_τ}: maximum torque bandwidth

$\omega_{MT_\tau}^{CIC}$: the maximum torque bandwidth for CIC

$\omega_{MT_\tau}^{inn}$: the upper frequency limit at which maximum torque generation is guaranteed and derived from the inner control path for CIC

$\omega_{MT_\tau}^{inn,lower}$: the lower frequency limit at which maximum torque generation is guaranteed and solely derived from the inner control path for CIC

$\omega_{MT_\tau}^{out}$: the upper frequency limit at which maximum torque generation is guaranteed and derived from the outer control path for CIC

ω_{LFB}: a measure that represents a feasible width in frequency ensuring generation of maximum output torque

ω_{MT_ω}: the maximum velocity bandwidth

$\omega_{MT_\omega}^{CIC}$: the maximum velocity bandwidth for CIC

$\omega_{MT_\omega}^{out}$: the upper frequency limit at which maximum velocity generation is guaranteed and derived from the outer control path for CIC

$\omega_{MT_\omega}^{inn}$: the upper frequency limit at which maximum velocity generation is guaranteed and derived from the inner control path for CIC

$\omega_{MT_\omega}^{inn,lower}$: the lower frequency limit at which maximum velocity generation is guaranteed and solely derived from the inner control path for CIC

τ_m: motor torque (control input)

τ_{fric}: friction torque at the motor side

τ_{ext}: external torque at the link side

τ_s: spring torque

$\tau_{mc,max}$: the maximum continuous motor torque

$\tau_{des,max}$: the maximum desired output torque

τ_{des}: desired output torque

θ: motor displacement

ϕ_{K_q}: tuples for $[K_q^i, \omega_{MT_\tau}^{out,i}]$

ϕ_{K_p}: tuples for $[K_p^i, \omega_{MT_\tau}^{inn,i}]$

$\phi_{K_p,lower}$: tuples for $[K_p^i, \omega_{MT_\tau}^{inn,lower,i}]$

$\boldsymbol{\phi_s}$: nonlinear mapping between spring deflection and force/torque

$\mathcal{H}_{spring}$: the mapping function from Z_{des} to Z_{spring}

$\mathcal{H}_{load}$: the mapping function from Z_{des} to Z_{load}

Bibliography

[1] Kyoungchul Kong, Joonbum Bae, and Masayoshi Tomizuka. "Control of rotary series elastic actuator for ideal force-mode actuation in human–robot interaction applications." In: *IEEE/ASME transactions on mechatronics* 14.1 (2009), pp. 105–118.

[2] Michiel Plooij and Martijn Wisse. "A novel spring mechanism to reduce energy consumption of robotic arms." In: *2012 IEEE/RSJ International Conference on Intelligent Robots and Systems*. IEEE. 2012, pp. 2901–2908.

[3] Samuel K Au, Jeff Weber, and Hugh Herr. "Biomechanical design of a powered ankle-foot prosthesis." In: *2007 IEEE 10th International conference on rehabilitation robotics*. IEEE. 2007, pp. 298–303.

[4] Ye Zhao et al. "Impedance control and performance measure of series elastic actuators." In: *IEEE Transactions on Industrial Electronics* 65.3 (2017), pp. 2817–2827.

[5] Patrick M Wensing et al. "Proprioceptive actuator design in the mit cheetah: Impact mitigation and high-bandwidth physical interaction for dynamic legged robots." In: *Ieee transactions on robotics* 33.3 (2017), pp. 509–522.

[6] Luigi Villani and J De Schutterm. *Handbook of robotics, chapter force control.* 2008.

[7] Neville Hogan. "Impedance control: An approach to manipulation: Part II—Implementation." In: (1985).

[8] Christian Ott et al. "On the passivity-based impedance control of flexible joint robots." In: *IEEE Transactions on Robotics* 24.2 (2008), pp. 416–429.

[9] Manuel Keppler et al. “A passivity-based approach for trajectory tracking and link-side damping of compliantly actuated robots.” In: *2016 IEEE International Conference on Robotics and Automation (ICRA)*. IEEE. 2016, pp. 1079–1086.

[10] Luca Martin. “Optimization of the Intrinsic Stiffnesses of a Robot with Variable-Stiffness-Actuators under External Disturbances with Respect to Control Effort.” PhD thesis. Technische Universität München, 2024.

[11] Jun Wu, Jinsong Wang, and Zheng You. “An overview of dynamic parameter identification of robots.” In: *Robotics and computer-integrated manufacturing* 26.5 (2010), pp. 414–419.

[12] Jan Swevers et al. “Optimal robot excitation and identification.” In: *IEEE transactions on robotics and automation* 13.5 (1997), pp. 730–740.

[13] Jonas Vantilt et al. “Optimal excitation and identification of the dynamic model of robotic systems with compliant actuators.” In: *2015 IEEE International Conference on Robotics and Automation (ICRA)*. IEEE. 2015, pp. 2117–2124.

[14] Sebastian Wolf and Maged Iskandar. “Extending a dynamic friction model with nonlinear viscous and thermal dependency for a motor and harmonic drive gear.” In: *2018 IEEE International Conference on Robotics and Automation (ICRA)*. IEEE. 2018, pp. 783–790.

[15] Wei Yin et al. “Design and parameters identification of flexible joint robot.” In: *2017 IEEE International Conference on Mechatronics and Automation (ICMA)*. IEEE. 2017, pp. 1297–1302.

[16] Alin Albu-Schäffer. “Regelung von Robotern mit elastischen Gelenken am Beispiel der DLR-Leichtbauarme.” PhD thesis. Technische Universität München, 2002.

[17] Luc Le-Tien. “Ansatze zur entkoppelten Regelung von mechanisch gekoppelten Doppelgelenken eines DLR-Medizinroboters.” PhD thesis. Dresden, Techn. Univ., 2010.

[18] V Held and Chr Maron. “Estimation of friction characteristics, inertial and coupling coefficients in robotic joints based on current and speed measurements.” In: *Robot Control 1988 (Syroco’88)*. Elsevier, 1989, pp. 207–212.

[19] J-W Choi, S-C Lee, and H-G Kim. "Inertia identification algorithm for high-performance speed control of electric motors." In: *IEE Proceedings-Electric Power Applications* 153.3 (2006), pp. 379–386.

[20] Maxime Gautier and Ph Poignet. "Extended Kalman filtering and weighted least squares dynamic identification of robot." In: *Control Engineering Practice* 9.12 (2001), pp. 1361–1372.

[21] Marouene Oueslati et al. "Improving the dynamic accuracy of elastic industrial robot joint by algebraic identification approach." In: *2012 1st International Conference on Systems and Computer Science (ICSCS)*. IEEE. 2012, pp. 1–6.

[22] Roger Miranda-Colorado and Javier Moreno-Valenzuela. "Experimental parameter identification of flexible joint robot manipulators." In: *Robotica* 36.3 (2018), pp. 313–332.

[23] Tim J Rogers et al. "On a grey box modelling framework for nonlinear system identification." In: *Special Topics in Structural Dynamics, Volume 6: Proceedings of the 35th IMAC, A Conference and Exposition on Structural Dynamics 2017*. Springer. 2017, pp. 167–178.

[24] K Worden et al. "Identification of pre-sliding and sliding friction dynamics: Grey box and black-box models." In: *Mechanical systems and signal Processing* 21.1 (2007), pp. 514–534.

[25] Erik Wernholt and Svante Gunnarsson. "Nonlinear identification of a physically parameterized robot model 1." In: *IFAC Proceedings Volumes* 39.1 (2006), pp. 143–148.

[26] Jonas Sjöberg et al. "Nonlinear black-box modeling in system identification: a unified overview." In: *Automatica* 31.12 (1995), pp. 1691–1724.

[27] Jiexin Zhang and Bo Zhang. "An iterative identification method for the dynamics and hysteresis of robots with elastic joints." In: *Nonlinear Dynamics* 111.15 (2023), pp. 13939–13953.

[28] Filipe Marques et al. "A survey and comparison of several friction force models for dynamic analysis of multibody mechanical systems." In: *Nonlinear Dynamics* 86 (2016), pp. 1407–1443.

[29] Jerzy Wojewoda et al. "Hysteretic effects of dry friction: modelling and experimental studies." In: *Philosophical Transactions of the Royal Society A: Mathematical, Physical and Engineering Sciences* 366.1866 (2008), pp. 747–765.

[30] Charles Augustin Coulomb. *Théorie des machines simples: en ayant égard au frottement de leurs parties, et à la roideur de cordages.* 1785.

[31] Brian Armstrong-Helouvry. *Control of machines with friction.* Vol. 128. Springer Science & Business Media, 1991.

[32] R Stribeck. "Die Wesentlichen Eigenschaften der Gleit-und Rollenlager [The key qualities of sliding and roller bearings]." In: *Z. Vereines Seutscher Ing.* 46 (1902), pp. 1432–1437.

[33] C Canudas De Wit et al. "A new model for control of systems with friction." In: *IEEE Transactions on automatic control* 40.3 (1995), pp. 419–425.

[34] P Dahl and A Solid Friction Model. "The Aerospace Corporation." In: *El Segundo, CA, Tech. Rep. TOR-0158 (3107-18)* (1968).

[35] Nguyen B Do, Aldo A Ferri, and Olivier A Bauchau. "Efficient simulation of a dynamic system with LuGre friction." In: (2007).

[36] Karl Johanastrom and Carlos Canudas-De-Wit. "Revisiting the LuGre friction model." In: *IEEE Control systems magazine* 28.6 (2008), pp. 101–114.

[37] R Van et al. "Compliant actuator designs. review of actuators with passive adjustable compliance/controllable stiffness for robotic applications." In: *IEEE Robotics Automation Magazine* 16.3 (2009), pp. 81–94.

[38] Gill A Pratt and Matthew M Williamson. "Series elastic actuators." In: *Proceedings 1995 IEEE/RSJ international conference on intelligent robots and systems. Human robot interaction and cooperative robots.* Vol. 1. IEEE. 1995, pp. 399–406.

[39] Daniel Paluska and Hugh Herr. "The effect of series elasticity on actuator power and work output: Implications for robotic and prosthetic joint design." In: *Robotics and Autonomous Systems* 54.8 (2006), pp. 667–673.

[40] Manuel Keppler et al. “Analyzing the performance limits of articulated soft robots based on the ESPi framework: Applications to damping and impedance control.” In: *IEEE Robotics and Automation Letters* 6.4 (2021), pp. 7121–7128.

[41] Andrea Calanca and Paolo Fiorini. “On the role of compliance in force control.” In: *Intelligent Autonomous Systems 13: Proceedings of the 13th International Conference IAS-13*. Springer. 2016, pp. 1243–1255.

[42] Chan Lee et al. “Generalization of series elastic actuator configurations and dynamic behavior comparison.” In: *Actuators*. Vol. 6. 3. MDPI. 2017, p. 26.

[43] Uwe Mettin et al. “Parallel elastic actuators as a control tool for preplanned trajectories of underactuated mechanical systems.” In: *The international journal of robotics research* 29.9 (2010), pp. 1186–1198.

[44] Philipp Beckerle et al. “Series and parallel elastic actuation: Influence of operating positions on design and control.” In: *IEEE/ASME Transactions on Mechatronics* 22.1 (2016), pp. 521–529.

[45] Tom Verstraten et al. “Series and parallel elastic actuation: Impact of natural dynamics on power and energy consumption.” In: *Mechanism and Machine Theory* 102 (2016), pp. 232–246.

[46] Mahdi Khoramshahi et al. “Natural dynamics modification for energy efficiency: A data-driven parallel compliance design method.” In: *2014 IEEE International Conference on Robotics and Automation (ICRA)*. IEEE. 2014, pp. 2412–2417.

[47] G. Tonietti, R. Schiavi, and A. Bicchi. “Design and Control of a Variable Stiffness Actuator for Safe and Fast Physical Human/Robot Interaction.” In: *Proceedings of the 2005 IEEE International Conference on Robotics and Automation*. 2005, pp. 526–531. DOI: 10.1109/ROBOT.2005.1570172.

[48] Bram Vanderborght et al. “Development of a compliance controller to reduce energy consumption for bipedal robots.” In: *Autonomous Robots* 24 (2008), pp. 419–434.

[49] Alin Albu-Schäffer et al. “Anthropomorphic soft robotics–from torque control to variable intrinsic compliance.” In: *Robotics Research: The 14th International Symposium ISRR*. Springer. 2011, pp. 185–207.

[50] Sebastian Wolf, Oliver Eiberger, and Gerd Hirzinger. "The DLR FSJ: Energy based design of a variable stiffness joint." In: *2011 IEEE international conference on robotics and automation*. IEEE. 2011, pp. 5082–5089.

[51] Werner Friedl et al. "Wrist and forearm rotation of the DLR hand arm system: Mechanical design, shape analysis and experimental validation." In: *2011 IEEE/RSJ international conference on intelligent robots and systems*. IEEE. 2011, pp. 1836–1842.

[52] Bram Vanderborght et al. "Variable impedance actuators: A review." In: *Robotics and autonomous systems* 61.12 (2013), pp. 1601–1614.

[53] Andrea Calanca, Riccardo Muradore, and Paolo Fiorini. "A review of algorithms for compliant control of stiff and fixed-compliance robots." In: *IEEE/ASME transactions on mechatronics* 21.2 (2015), pp. 613–624.

[54] Daniel E Whitney. "Force feedback control of manipulator fine motions." In: (1977).

[55] Marc H Raibert and John J Craig. "Hybrid position/force control of manipulators." In: (1981).

[56] Matthew T Mason. "Compliance and force control for computer controlled manipulators." In: *IEEE Transactions on Systems, Man, and Cybernetics* 11.6 (1981), pp. 418–432.

[57] Bruno Siciliano et al. *Force control*. Springer, 2009.

[58] Sehoon Oh and Kyoungchul Kong. "High-precision robust force control of a series elastic actuator." In: *IEEE/ASME Transactions on mechatronics* 22.1 (2016), pp. 71–80.

[59] Wolfgang F Rampeltshammer, Arvid QL Keemink, and Herman Van Der Kooij. "An improved force controller with low and passive apparent impedance for series elastic actuators." In: *IEEE/ASME transactions on mechatronics* 25.3 (2020), pp. 1220–1230.

[60] Zhijun Li et al. "sEMG-based joint force control for an upper-limb power-assist exoskeleton robot." In: *IEEE journal of biomedical and health informatics* 18.3 (2013), pp. 1043–1050.

[61] Heike Vallery et al. “Compliant actuation of rehabilitation robots.” In: *IEEE Robotics & Automation Magazine* 15.3 (2008), pp. 60–69.

[62] Andrea Calanca, Riccardo Muradore, and Paolo Fiorini. “Impedance control of series elastic actuators: Passivity and acceleration-based control.” In: *Mechatronics* 47 (2017), pp. 37–48.

[63] Hyunwook Lee et al. “Robust Elastic Structure Preserving Control for High Impedance Rendering of Series Elastic Actuator.” In: *IEEE Robotics and Automation Letters* 9.4 (2024), pp. 3601–3608.

[64] Dongwon Kim et al. “A robust impedance controller design for series elastic actuators using the singular perturbation theory.” In: *IEEE/ASME Transactions on Mechatronics* 25.1 (2019), pp. 164–174.

[65] Rahul Mallik. “Robust Control Approaches for Minimizing the Bandwidth Ratio in Multi-Loop Control.” In: *arXiv preprint arXiv:2203.09022* (2022).

[66] Manuel Keppler et al. “Elastic structure preserving (ESP) control for compliantly actuated robots.” In: *IEEE Transactions on Robotics* 34.2 (2018), pp. 317–335.

[67] Manuel Keppler et al. “Elastic structure preserving impedance (ESπ) control for compliantly actuated robots.” In: *2018 IEEE/RSJ International Conference on Intelligent Robots and Systems (IROS)*. IEEE. 2018, pp. 5861–5868.

[68] Alin Albu-Schäffer, Christian Ott, and Gerd Hirzinger. “A unified passivity-based control framework for position, torque and impedance control of flexible joint robots.” In: *The international journal of robotics research* 26.1 (2007), pp. 23–39.

[69] Dylan P Losey et al. “A time-domain approach to control of series elastic actuators: Adaptive torque and passivity-based impedance control.” In: *IEEE/ASME Transactions on Mechatronics* 21.4 (2016), pp. 2085–2096.

[70] Wesley Roozing et al. “Comparison of open-loop and closed-loop disturbance observers for series elastic actuators.” In: *2016 IEEE/RSJ International Conference on Intelligent Robots and Systems (IROS)*. IEEE. 2016, pp. 3842–3847.

[71] Abner Asignacion et al. “High-stiffness control of series elastic actuators using a noise reduction disturbance observer.” In: *IEEE Transactions on Industrial Electronics* 69.8 (2021), pp. 8212–8219.

[72] Chan Lee and Sehoon Oh. “Performance analysis of series elastic actuator based on maximum torque transmissibility.” In: *IEEE Transactions on Control Systems Technology* 30.1 (2021), pp. 392–399.

[73] Chan Lee, Wiha Choi, and Sehoon Oh. “Maximum torque generation of SEA under velocity control.” In: *2016 IEEE 14th international workshop on advanced motion control (AMC)*. IEEE. 2016, pp. 16–23.

[74] J Edward Colgate and J Michael Brown. “Factors affecting the z-width of a haptic display.” In: *Proceedings of the 1994 IEEE International Conference on Robotics and Automation*. IEEE. 1994, pp. 3205–3210.

[75] Nick Colonnese and Allison M Okamura. “M-Width: Stability, noise characterization, and accuracy of rendering virtual mass.” In: *The International Journal of Robotics Research* 34.6 (2015), pp. 781–798.

[76] Christopher I Byrnes, Alberto Isidori, Jan C Willems, et al. “Passivity, feedback equivalence, and the global stabilization of minimum phase nonlinear systems.” In: *IEEE Transactions on automatic control* 36.11 (1991), pp. 1228–1240.

[77] Heike Vallery et al. “Passive and accurate torque control of series elastic actuators.” In: *2007 IEEE/RSJ international conference on intelligent robots and systems*. IEEE. 2007, pp. 3534–3538.

[78] Hyunwook Lee et al. “Relaxing the conservatism of passivity condition for impedance controlled series elastic actuators.” In: *2019 IEEE/RSJ International Conference on Intelligent Robots and Systems (IROS)*. IEEE. 2019, pp. 7610–7615.

[79] David William Robinson. “Design and analysis of series elasticity in closed-loop actuator force control.” PhD thesis. Massachusetts Institute of Technology, 2000.

[80] Jerry E Pratt and Benjamin T Krupp. “Series elastic actuators for legged robots.” In: *Unmanned Ground Vehicle Technology VI*. Vol. 5422. SPIE. 2004, pp. 135–144.

[81] Anton Shu et al. "Impact Robustness vs. Torque Bandwidth: A Design Guide for Differential Elastic Actuators." In: *IEEE Transactions on Robotics* (2024).

[82] Arion Pons and Tsevi Beatus. "Band-type resonance: non-discrete energetically optimal resonant states." In: *Nonlinear Dynamics* 111.2 (2023), pp. 1161–1192.

[83] Arion Pons and Tsevi Beatus. "Elastic-bound conditions for energetically optimal elasticity and their implications for biomimetic propulsion systems." In: *Nonlinear Dynamics* 108.3 (2022), pp. 2045–2074.

[84] James R Barber and M Ciavarella. "Contact mechanics." In: *International Journal of solids and structures* 37.1-2 (2000), pp. 29–43.

[85] Eldison Dimo and Andrea Calanca. "A Passive, Accurate and Model-Free Friction Observer Suitable for Force Control Applications." In: *Authorea Preprints* (2024).